
A Review of NEST Models for Liquid Xenon & Exhaustive Comparison to Other Approaches

M. Szydagis^{1,*}, **J. Balajthy**^{2,3}, **G.A. Block**^{1,4,5}, **J.P. Brodsky**⁶, **E. Brown**⁴,
J.E. Cutter^{2,7}, **S.J. Farrell**⁸, **J. Huang**^{2,9}, **A.C. Kamaha**^{1,10}, **E.S. Kozlova**¹¹,
C.S. Liebenthal⁸, **D.N. McKinsey**^{12,13}, **K. McMichael**⁴, **R. McMonigle**¹,
M. Mooney¹⁴, **J. Mueller**¹⁴, **K. Ni**⁹, **G.R.C. Rischbieter**^{1,15,17,*}, **K. Trengove**^{1,10},
M. Tripathi², **C.D. Tunnell**⁸, **V. Velan**¹², **S. Westerdale**¹⁶, **M.D. Wyman**¹,
Z. Zhao⁹, and **M. Zhong**⁹

¹*Department of Physics, University at Albany, State University of New York, Albany, NY, USA*

²*Department of Physics, University of California Davis, Davis, CA, USA*

³*Sandia National Laboratories, Livermore, CA, USA*

⁴*Department of Physics, Applied Physics and Astronomy, Rensselaer Polytechnic Institute, Troy, NY, USA*

⁵*Department of Physics and Astronomy, University of New Mexico, Albuquerque, NM, USA*

⁶*Lawrence Livermore National Laboratory, Livermore, CA, USA*

⁷*Deepgram, Mountain View, CA, USA*

⁸*Department of Physics and Astronomy, Rice University, Houston, TX, USA*

⁹*Department of Physics, University of California San Diego, La Jolla, CA, USA*

¹⁰*Department of Physics and Astronomy, University of California Los Angeles, Los Angeles, CA, USA*

¹¹*ORCID: 0000-0002-1976-3425*

¹²*Lawrence Berkeley National Laboratory, Berkeley, CA, USA*

¹³*Department of Physics, University of California Berkeley, Berkeley, CA, USA*

¹⁴*Department of Physics, Colorado State University, Fort Collins, CO, USA*

¹⁵*Department of Physics, University of Michigan, Ann Arbor, MI, USA*

¹⁶*Department of Physics & Astronomy, University of California Riverside, Riverside, CA, USA*

¹⁷*Physik-Institut, University of Zürich, Zürich, Switzerland*

Correspondence*:

Matthew Szydagis

Department of Physics,

University at Albany, State University of New York,

1400 Washington Av., Albany, NY 12222, USA

mszydagis@albany.edu

Gregory R.C. Rischbieter

Department of Physics, University of Michigan,

450 Church Street, Ann Arbor, MI 48109, USA

rischbie@umich.edu

ABSTRACT

This paper will discuss the microphysical simulation of interactions in liquid xenon, the active detector medium in many leading rare-event searches for new physics, and describe experimental observables useful for understanding detector performance. The scintillation and ionization yield distributions for signal and background will be presented using the Noble Element Simulation Technique (NEST), which is a toolkit based on experimental data and simple, empirical formulae, which mimic previous microphysics modeling, but are guided by data. The NEST models for light and charge production as a function of the particle type, energy, and electric field will be reviewed, as well as models for energy resolution and final pulse areas. NEST will be compared to other models or sets of models, and vetted against real data, with several specific examples pulled from XENON, ZEPLIN, LUX, LZ, PandaX, and table-top experiments used for calibrations.

Keywords: WIMP dark matter direct detection, liquid Xenon, simulations/models

1 INTRODUCTION

For the past 15+ years, leading results in dark matter direct detection searches have come from detectors based on the principle of the dual-phase TPC (Time Projection Chamber) using a liquefied noble element as the detection medium [1]. Liquid xenon (LXe) TPCs have in particular produced the most stringent cross-section constraints, for spin-independent (SI) as well as neutron spin-dependent (SD) interactions between WIMPs (Weakly Interacting Massive Particles) and xenon nuclei. More recently, usage of LXe has also led to WIMP limits using different EFT (Effective Field Theory) operators, for mass-energies above $O(5 \text{ GeV})$ [2]. EFTs extend the set of allowable operators beyond the standard SI and SD interactions, and include searches at higher nuclear recoil energies. Unrelated to dark matter, electron-recoil searches up to the MeV regime have set strict constraints on $0\nu\beta\beta$ decay [3], and led to seeing double e^- capture [4]. XENONnT and PandaX have recently illustrated the potential for precision measurements of ^8B [5, 6].

To interpret results from past, present, and future experiments, a reliable MC (Monte Carlo) simulation is required. Recent works have demonstrated the utility of NEST, the cross-disciplinary, detector-agnostic MC software reviewed here [7, 8, 9], for a variety of active detector materials: LAr [10, 11, 12] and GXe, but especially LXe. As the multi-tonne-scale TPCs have commenced data collection [13, 8, 9], improved MC techniques will not only assist in limit setting, but will be needed for extracting dark matter particle mass and cross section in the event of a WIMP discovery. In either scenario, or for the design of a new TPC, predictions of performance are needed on key metrics like the fundamental scintillation light and ionization charge yields for LXe, the focus of this work. NEST v2.4 is its default; different versions are specified as needed. This manuscript is a technical overview of updates to NEST, including new models and comparisons. More pedagogical reviews of the models and related physics are available in [14, 15].

Section 2.1 contains mean scintillation and ionization yields of electronic recoil (ER) backgrounds, with comparisons to data. These underlie the ER background (BG) models in Xe-based dark matter detectors. Section 2.2 summarizes the methods for varying these mean yields to model realistic fluctuations, with variation in the total number of quanta (light and charge) produced. Section 2.3 has the yields of nuclear recoils (NR) and their fluctuations. These form the foundation for the signal model in a LXe-based dark matter search, as well as for NR backgrounds (from fast neutron scattering and coherent elastic neutrino-nucleus scattering, CE ν NS). Lastly, Section 3 compares NEST's modeling of mean yields (Sections 2.1 and 2.3) to past and present approaches in existing literature, including some first-principles ones, before the conclusion. The strengths and weaknesses of the different approaches will be summarized, underscoring NEST's ability to model data across a broad range of energies and electric fields phenomenologically.

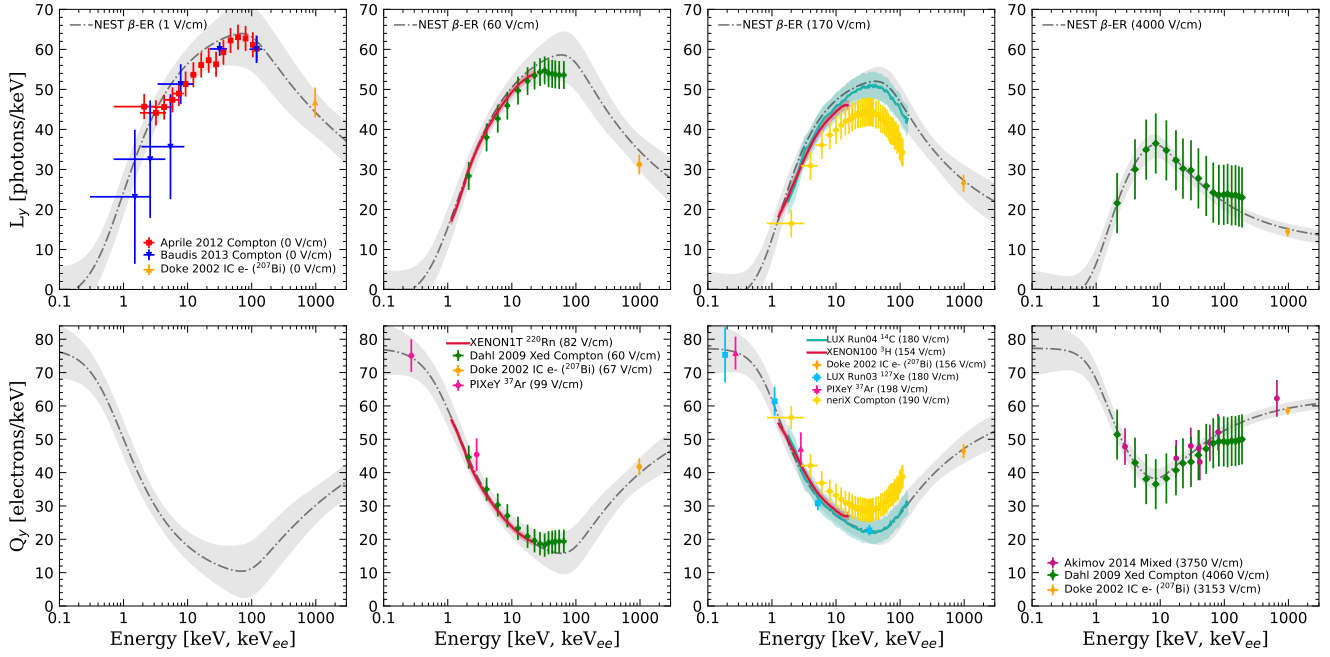


Figure 1. β electron recoil (ER) L_y (top row) and Q_y (bottom row) vs. energy E . Different fields \mathcal{E} are represented, from 0 V/cm (left column) to the highest fields for which data exist at multiple E s, $\sim 3\text{--}4$ kV/cm (right column). More data exist, all of which are utilized to inform NEST, but these are selected as representative examples of the lowest and highest \mathcal{E} s and lowest and highest E s, from sub-keV to 1 MeV across different types of experiments [16, 17, 18, 19, 20, 21, 22, 23, 24, 25, 26]. MC lines are black dashed with gray 1σ error bands. Newer results e.g. XENON1T's ^{220}Rn calibration illustrate the predictive power of NEST, using the latest β model which stems largely from ^{14}C decays [22, 27].

2 MICROPHYSICS MODELING EVALUATION

NEST model choices were justified earlier (in [15] and in references therein) but are re-evaluated herein more comprehensively, with more, newer data. NEST is openly shared, allowing for regular re-evaluation using the latest calibrations [28]. While such data often provide relative light and charge yields, these are converted to absolute yields if the detector gains are calculable, known as g_1 and g_2 for those respective yields. The light yield gain, g_1 , is the primary photon detection efficiency, while the charge gain, g_2 , is the average signal size per e^- escaping the interaction site. Uncertainties in these gains are a significant source of systematic uncertainty, but newer data from higher-quality calibrations mitigate this. Combining calibration data ranging from < 1 keV to > 1 MeV energy, NEST has predictive shapes for the primary scintillation and ionization yields as functions of energy, E , and drift electric field, \mathcal{E} , for different particle interaction types [29]. The status of the NEST modeling of these shapes is shown in Figure 1.

2.1 Electronic Recoils (Betas, Gammas, X Rays)

NEST begins with a model of the sum total yield, summing the VUV (vacuum ultraviolet) scintillation photons and ionization electrons produced. IR photons are not included, as their yield in LXe is lower by a factor of ~ 4 [30], and their wavelength is beyond the sensitivity of most photon sensors in common use in dark matter experiments at least. The work function, W_q , for production of quanta depends only upon the density, using a linear fit based on data collected in [31], across phases (see also Appendix A):

$$W_q [eV] = 21.94 - 2.93\rho = \frac{W_i}{1 + N_{ex}/N_i}. \quad (1)$$

ρ is the mass density in units of g/cm^3 . LXe TPCs typically operate at temperatures of 165–180 K, and pressures of 1.5–2 bar(a), leading to $\rho \approx 2.9 \text{ g/cm}^3$ and resulting in a W_q of between 13–14 eV (Eqn. 1, with discrepant values discussed in [32]). The exciton-ion ratio or N_{ex}/N_i relates W_q with the work function for ionization, W_i , which was defined for charge yields. Moreover, N_{ex}/N_i determines a pre-recombination (ions and e^- s) split of quanta into light and charge (see Appendix A, where the ρ dependence is explained):

$$N_{ex}/N_i = (0.0674 + 0.0397\rho) \times \text{erf}(0.05E), \quad (2)$$

where E is deposited energy in keV, for a β interaction or Compton scatter, and ‘erf’ refers to the error function. Here, the ρ dependence is based again on [31] while the E dependence comes from reconciling [18, 33, 34], given evidence that light yield approaches zero as energy E decreases, with lower- E data sets favoring both less recombination and smaller N_{ex}/N_i . Ionization electrons can recombine with Xe atoms or can escape from the interaction site entirely. Therefore, the number of photons N_{ph} is not simply equal to N_{ex} , providing an anti-correlation in the observed light and charge yields, motivating the use of both charge and light to measure the energy, $E = W_q (N_{ph} + N_{e^-})$ [15]:

$$N_{ph} = [N_{ex} + r(E, \mathcal{E}, \rho)N_i] = S1 / g_1 \quad \text{and} \quad N_{e^-} = [1 - r(E, \mathcal{E}, \rho)]N_i = S2 / g_2, \quad (3)$$

where r is recombination probability for e^- -ion pairs depending on E , \mathcal{E} , and ρ , as well as particle and interaction type, and the S1 and S2 are the experimental observables. Typical values of g_1 are ~ 0.1 , but $O(10)$ for g_2 due to secondary (gas) scintillation (g_2 is 0.5–1 in single-phase TPCs). The light and charge yields per unit energy are traditionally quoted in experiment, defined as $L_y \equiv N_{ph}/E$ and $Q_y \equiv N_{e^-}/E$.

Q_y is modeled first; L_y is set by W_q and subtraction:

$$N_q \equiv N_{ex} + N_i = N_{ph} + N_{e^-} = E / W_q, \quad \text{where} \quad N_{e^-} = Q_y E, \quad \text{and} \quad N_{ph} = N_q - N_{e^-}, \quad (4)$$

where N_q is the total quanta. This procedure leverages the greater reliability of S2 measurements *cf.* S1 for lower E , as explained in [24, 15]. Q_y in the ER model is a sum of two sigmoids:

$$Q_y(E, \mathcal{E}) = m_1(\mathcal{E}) + \frac{m_2 - m_1(\mathcal{E})}{[1 + (\frac{E}{m_3(\mathcal{E})})^{m_4(\mathcal{E})}]^{m_9}} + m_5(\mathcal{E}) - \frac{m_5(\mathcal{E})}{[1 + (\frac{E}{m_7(\mathcal{E})})^{m_8}]^{m_{10}(\mathcal{E})}}, \quad (5)$$

with m_1 serving as the minimum field-dependent charge yield. m_2 determines the low- E behavior, and m_7 controls the field dependence at high energies. The individual m_i are summarized within Appendix B (with [27] providing more details). While empirical, the first (left, m_1 +...) and second (right, $+m_5$...) sigmoids of Equation 5 capture the qualitative behavior of two first-principles options, respectively: the Thomas-Imel box model at low energies [35], and Doke-modified Birks’ Law at higher energies [36]. Between ~ 15 keV and the energy of a MIP (minimally ionizing particle) within Xe (about 1 MeV), a track shape is described as cylindrical by Doke for modeling the recombination, and the dE/dx decreases with increasing E . The recombination probability r decreases as energy E increases, reducing the ratio of L_y to Q_y [37, 14, 38]. Below ~ 15 keV, deposits are more amorphous, and straight 1-D track lengths become ill-defined: r and L_y increase with the 3-D ionization density and the energy, as dE/dx increases with E .

A Thomas-Imel approach historically uses E and models energy deposits within symmetric boxes or spheres, while the Doke / Birks’ Law uses dE/dx and assumes long tracks (cylinders). The former will exhibit r (and therefore L_y) only increasing with energy, the latter decreasing usually (Q_y anti-correlated).

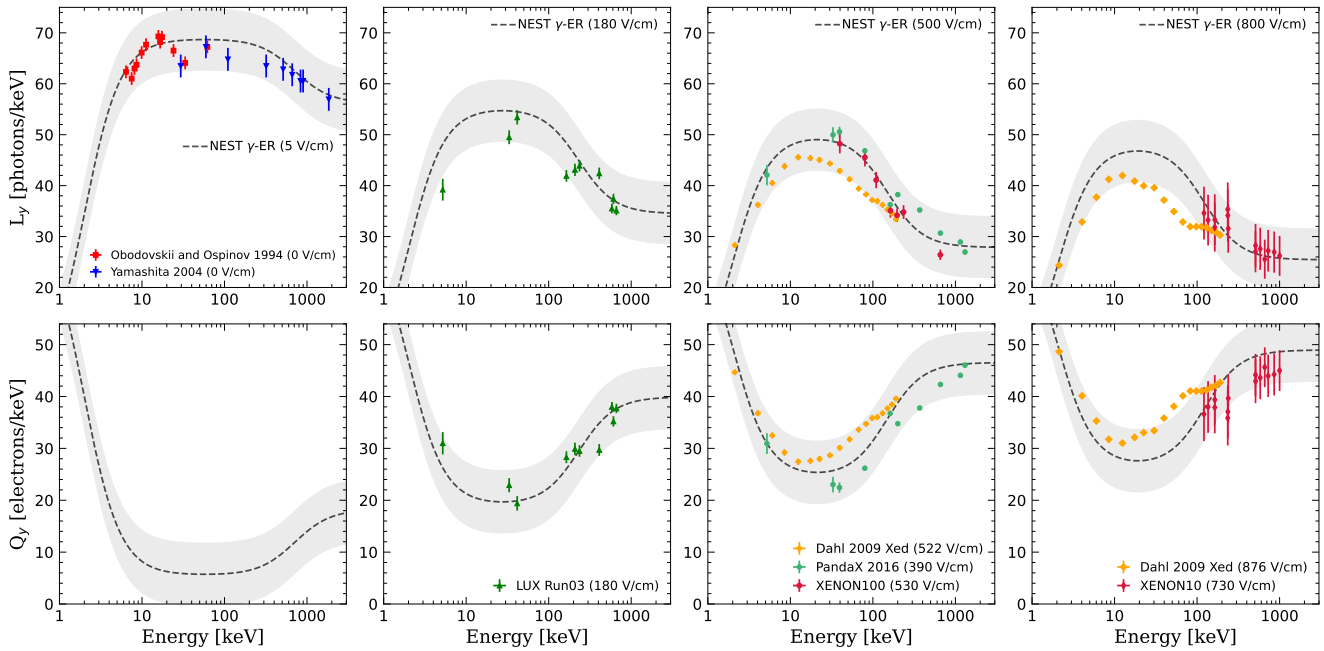


Figure 2. γ ER L_y (top row) and Q_y (bottom) vs. E at $\mathcal{E} = 0$ (left) to nearly 10^3 V/cm (right). Before β calibrations were common, photoabsorption peaks from monoenergetic γ s were used [39, 40, 41, 20, 42, 43, 44]. At sufficiently high E , L_y is higher and Q_y lower than in Fig. 1, as some unresolvable multiple scattering occurs, treated as single scattering in NEST [45]. Multiple lower- E , higher- dE/dx vertices are “averaged over.” Low fields again approximate 0 V/cm, when NEST becomes singular. As in other plots gray 1σ bands are driven by data errors, model shape constraints (sigmoidal), and monotonic \mathcal{E} dependence. LUX L_y points, but not Q_y , seem systematically low due to a different W_q applied, with LUX assuming 13.7 eV (no ρ dependence). Dahl data sets exhibit different shapes due to being mixtures of Compton scatters and photoabsorption.

The recombination fraction or probability, r , is found retroactively in recent NEST versions after fitting to Q_y per Equation 5, chosen for matching both the box and Birks models. Using Equation 2 as a constraint avoids the degeneracy of this r with N_{ex}/N_i , with the sum $N_{ex} + N_i$ (also equal to $N_{ph} + N_{e-}$) already constrained by Equations 1 and 4 – the former determines W_q and the latter total quanta N_q based on W_q . Any change in W_q (one work function averaging over individual work functions for photon and electron production) should change L_y and Q_y equally, preserving both their shapes in both energy and field [46].

Figure 1 summarizes both L_y and Q_y for β s and for Compton scattering ERs from both data and NEST, with NEST using a typical LXe operating condition of $\rho = 2.89$ g/cm³ ($T = 173$ K, $P = 1.57$ bar). The non-monotonic energy dependence is obvious. Meanwhile, the L_y decreases from left to right (top) and Q_y correspondingly increases (bottom) as field increases, suppressing recombination at a fixed N_q . But even at $\mathcal{E} = 0$ there exists a “phantom” Q_y likely caused by an extreme delay in recombination, as explained in [18, 15], and repeated here: this is unobservable, except via long S1 integration times and by noting L_y vs. energy is the same shape at all fields, even 0. That implies a continuous change in L_y as $\mathcal{E} \rightarrow 0$. Non-0 fields standing in for 0 represent residual stray fields in a detector and/or inherent fields of Xe atoms [45].

Absorption of any high-energy photon, a γ or x-ray, is modeled like β interactions and Compton scatters, but with unique m_i (Figure 2), to capture sub-position-resolution multiple scatters and distinct dE/dx . L_y is mostly lower and Q_y higher for β s, as explained within the Figure 2 caption. While it might be possible to merge the γ and β models by relying on differences in dE/dx , γ s are treated independently at present. Appendix B lists the β and γ model parameters, in addition to those for NR models.

2.2 Yield Fluctuations

Energy resolution typically refers to Gaussian spreads (σ or FWHM) of monoenergetic peaks from high-energy γ -ray photoabsorption, but this is also relevant for lower energies, in WIMP searches. Smearing of continuous ER spectra can drive an increase in signal-like background events. But to understand statistical limitations for high-level parameters like monoenergetic-peak σ s or background discrimination we must start with lower-level parameters behind all the relevant stochastic processes involved. This modeling is discussed in depth in [15], but portions germane to this work are summarized in this section, culminating in a subsection enumerating the practical steps taken within the NEST code on git.

2.2.1 Total Quanta: Correlated Fluctuations

Realistic smearing of mean yields begins with a Fano-like factor, F_q , applied to the total quanta, N_q , prior to differentiation into N_{ex} and N_i . It is labeled as Fano-like, as it does not follow the strict sub-Poissonian definition [47]. F_q may exceed 1, but it is still used in the usual definition of the standard deviation of N_q , utilized for decades by Xe experiments to fit their data on combined- E (N_{ph} and N_{e-}) scale resolution:

$$\sigma_q = \sqrt{F_q \langle N_q \rangle}, \quad (6)$$

where F_q is defined for light and charge together as

$$F_q = 0.13 - 0.030\rho - 0.0057\rho^2 + 0.0016\rho^3 + \delta_F \sqrt{\langle N_q \rangle} \sqrt{\mathcal{E}}. \quad (7)$$

The first part of Equation 7 is a spline of data [31] from gas, liquid, and solid. The constant 0.13 represents the theoretical value of the Xe Fano factor following the traditional definition ($F_q < 1$). $O(0.1)$ matches NEXT gas data on N_{e-} [48] and Biagi's Degrad work. The second part of Eqn. 7 is only for liquid and is data-driven, where $\delta_F = 0.0015$ for LXe but is identically 0 for gaseous Xe. The $\sqrt{\langle N_q \rangle}$ term is included in order to match the data at MeV scales (*e.g.*, for $0\nu\beta\beta$ searches). Such results did not achieve the theoretical minimum in energy resolution even when reconstructing N_q , utilizing both channels of information (light and charge), instead of only a single channel. This was true even for the cases where the noise was allegedly subtracted or modeled [49, 50]. As Q_y increases with \mathcal{E} , the combined E resolution improves. However, the improvement is smaller than naïvely predicted, requiring the $\sqrt{\mathcal{E}}$ term in F_q to match the data [51, 52].

There are many possible explanations for this F_q becoming $\gg 1$ as E or \mathcal{E} changes. W_q may need to be replaced with separate W_{ex} and W_i for the excitation and ionization processes (both inelastic scattering), then further subdivided into different values that depend upon e^- energy shell. Lastly, elastic scattering of orbital e^- s may play a role. Mechanisms are discussed in [53] but explicit Fano-factor variations can be found in [15]. In NEST, a Gaussian smearing, constrained to be non-negative, is applied to N_q of width defined by Eqn. 6: $N_q = G[\langle N_q \rangle, \sigma_q]$. A binomial distribution then divides quanta into excitons versus ions.

2.2.2 Anti-Correlated Excitation and Recombination Fluctuations

F_q drives resolution on a combined- E scale, but such a scale is more relevant for monoenergetic peaks than dark matter searches [20, 15]. "Recombination fluctuations," however, describe the redistribution of N_{ph} and N_{e-} caused by widths paired with the means of Equation 3 or 4. Often conflated with excitation fluctuations (Equation 2), these are all fundamental and do not originate from detector effects [44, 41], and constitute one of the key factors for characterization of ER discrimination [54]. Moreover, they are not binomial, despite recombination (or, escape) appearing to be a binary decision. Potential explanations for this phenomenon include other energy loss mechanisms, or other effects which break the independence of draws, for instance δ -ray production (as observed at different energies in both Ar and Xe [55, 56]), the statistics of columnar recombination [57], and short-lived clustering of Xe dimers [58].

While it is unclear which explanation is correct, NEST proceeds with a fully empirical approach to simply model what is observed in data; following [41, 27] closely, NEST defines recombination variance as:

$$\sigma_r^2 = \langle r \rangle (1 - \langle r \rangle) N_i + \sigma_p^2 N_i^2, \quad \text{where } \sigma_r \approx \sigma_{N_{e^-}} \approx \sigma_{N_{ph}} \quad (\text{for small } F_q),$$

$$\sigma_p = A(\mathcal{E}) e^{-\frac{(\langle y \rangle - \xi)^2}{2\omega^2}} \left[1 + \text{erf}\left(\alpha_p \frac{\langle y \rangle - \xi}{\omega\sqrt{2}}\right) \right], \quad \text{and the } e^- \text{ fraction } y = N_{e^-}/N_q \text{ and } \langle y \rangle = Q_y W_q. \quad (8)$$

The $\langle r \rangle (1 - \langle r \rangle) N_i$ in σ_r follows the binomial expectation of $\sigma_r \propto \sqrt{N_i}$. The σ_p term leads to $\sigma_r \propto N_i$, as proposed in [54]. σ_p is a skewed Gaussian (on the second line) with field-dependent amplitude, A , varying from 0.05–0.1, as needed to simulate the spectral broadening of ER with higher drift electric field [27, 59]. In NEST versions < 2.1, σ_p was simulated as a constant, similar in value to A , but this was found to be inadequate for capturing the full behavior of recombination fluctuations [41].

σ_p 's dependent variable was chosen to be the mean electron fraction $\langle y \rangle$ for simplicity, as it is closely related to $1 - \langle r \rangle$. Recombination probability, defined within Equation 3, is degenerate with N_{ex}/N_i , while y is directly measurable. It can be written in terms of r : $y = (1 - r)/(1 + N_{ex}/N_i)$ [20]. Non-binomial fluctuations decrease as y approaches 0 or 1, causing σ_p to vanish. ξ , ω , and α_p are the centroid, width, and skew of σ_p , respectively. Default NEST values determining respectively the width and skewness of σ_p are $\omega = 0.2$ and $\alpha_p = -0.2$. (Future work may recast all of σ_r entirely in terms of y , not just σ_p .)

A skew centroid $\xi \approx 0.4$ – 0.5 was found based on β and γ data. The types of data included continuous spectra and monoenergetic-peak energy resolutions, both at multiple fields and energies [20, 44, 54]. ξ 's value depends on which data sets are used and which other parameters are fixed. A ξ near 0.5 leads to a maximum in σ_p (within σ_r) near $y = 0.5$, as would occur within a regular binomial distribution. The asymmetric shape σ_p is motivated by observations in recombination fluctuations at lower values of y (low field, high energy) compared to higher values of y (high field, low energy) [60, 54, 27].

Longer, less technical descriptions of all the steps within Section 2.2.2 are in [27, 60].

2.2.3 Recombination Skewness

We note here that the skewed Gaussian $\sigma_p(y)$ must not be conflated with the E and \mathcal{E} -dependent skew defined in Section IVB of [59] as α_r , as that skew is instead the observed asymmetry of the resultant charge yields. NEST uses α_r from Equation (13) in [59] to smear the mean N_{e^-} , while α_p controls the variance of recombination fluctuations, σ_r from Equation 8.

A positive α_r value can lead to better background discrimination than expected for a WIMP search that uses LXe. Weak rejection was expected due to the recombination fluctuations being greater (worse) than binomial, but positive α_r will shift ER events preferentially away from NR (more Q_y). This has already been observed [59].

2.2.4 Uncorrelated Fluctuations: Detector Effects (Known and Unknown)

Lastly, while the simulated σ_q widths predict correlated changes in S1 (L_y) and S2 (Q_y), and σ_r leads to anti-correlated change, uncorrelated noise also exists, affecting S1 and S2 independently. S1 and S2 gains are understood sources, assuming position-dependent light collection and field non-uniformities are taken into account. Unknown sources are modeled with a Gaussian smearing proportional to the pulse areas [32]. A quadratic term may be necessary at the MeV scale [58]. ER and NR are equally affected by any detector effects (known/unknown). The final E resolutions vs. E are seen for ER, NR, or both in [7, 32], supplementing validation of means in our Figures 1, 2, and 3 with their vetting of fluctuations. The scale of the unknown detector effects across experiments is 1–10% [32, 15, 61] (for S2s, and for non-integer forms of S1s, but effectively 0% for a spike count of S1 photons). See again Appendix A.

2.2.5 Computational Implementation

NEST is publicly available as a GitHub repository which includes the source code, interface scripts, and examples. It is C++ based, but can be run by dedicated scripts using either C++ or Python available on the repo. These can be used to generate expectation values of yields and their fluctuations for different detectors using Xe or Ar. The step-by-step procedure that NEST uses to do the latter is summarized below:

- F_q is used to determine the σ_q for a normal distribution of total (initially undifferentiated) ER quanta which can be considered “correlated noise,” because in this case N_{ph} and N_{e-} rise and fall together (Eq. A1 [62]). Two distinct F s exist for NR N_{ex} and N_i , breaking that correlation (Section 2.3).
- ER quanta are differentiated (N_{ex} and N_i) using a binomial distribution (Eq. A2 [62]), approximated as normal for computational speed, using the same Box-Müller algorithm as in the first bullet above. Any non-binomial / non-Gaussian fluctuation at this stage is essentially degenerate with the next step.
- A normal or skew-normal (Eq. 8–12 in [59]) in N_{e-} capped at N_q (min of 0) enforces the anti-correlated fluctuation of N_{ph} versus N_{e-} . This step was mismodeled in the past by uncorrelated Fano factors. The variance σ_r^2 has components proportional to both N_i (“binomial style”) and N_i^2 (data-driven).

Two more lists cover detector specifics for S1 and S2, closely following Appendix C of [62]. First, S1:

- S1.1 A binomial distribution with probability g_1 (3-D spatially varying) determines the fraction of N_{ph} successfully detected by photo-sensors; g_1 represents the product of geometric \times quantum efficiencies.
- S1.2 Single photo-electrons in sensors are modeled by 0-truncated Gaussians of sensor-specific width. Spike counting is emulated by means of artificially reduced width but non-zero for matching real data.
- S1.3 An if-else structure determines whether a second photo-electron is produced due to the 2PE effect. This step and S1.2 are Gaussian-approximated at high E in “hybrid” mode, or any E in “parametric.”
- S1.4 Geant4 (G4), Chroma, OptiX, or some other ray-tracer, or NEST’s built-in analytic-approximation ability simulates photon arrival times at S1 sensors and dictates whether a sufficient number of photons were detected in MC with above-threshold (experiment DAQ-specific) pulse areas, based upon S1.2+3.

The procedure to model the charge signal or S2 is more intricate, especially in a two-phase experiment:

- S2.1 Electrons (numbered N_{e-}) diffuse, transversely and longitudinally, as they drift at a drift speed determined by the liquid field but also density, and possibly temperature and pressure separately (the same applies to diffusion “constants”). Data-driven functions exist for all these phenomena in NEST.
- S2.2 An electron survival fraction is set by an exponential function depending on the originating depth in a detector and a characteristic electron MFP. It is used as the probability in a binomial distribution.
- S2.3 Another binomial distribution is utilized to find how many electrons survive extraction from the liquid to the gas. The efficiency is a function of the gas field \mathcal{E}_g between the liquid/gas boundary and the gate grid. NEST offers many options of asymptotic (1 at infinite \mathcal{E}_g) function based upon past data.
- S2.4 Each extracted electron produces Y_{e-} S2 photons based on the parameterization in [63] depending on \mathcal{E}_g , gas ρ , and the gap between the liquid surface and gate (thus \mathcal{E}_g comes into play twice). Y_{e-} is the mean of an int-rounded Gaussian of width $\sqrt{F_{S2}Y_{e-}}$. F_{S2} is $O(1)$ and captures grid non-uniformity.
- S2.5 A binomial of probability g_1^{gas} (2-D varying) like g_1 (liquid) begins a process similar to S1.1–4.

More precise S2 simulation is possible in the optional integration of Garfield with NEST, which also possesses an optional G4 integration for simulating E deposits prior to the first step above. More details on the lists here can be found in Section 2.2 of [15]. Section 2.2.4 explains NEST’s last layer. All values for the first list are in Table S4 (Appendix B) and examples for S1 and S2 in [60] especially in its Fig. 4.3 left.

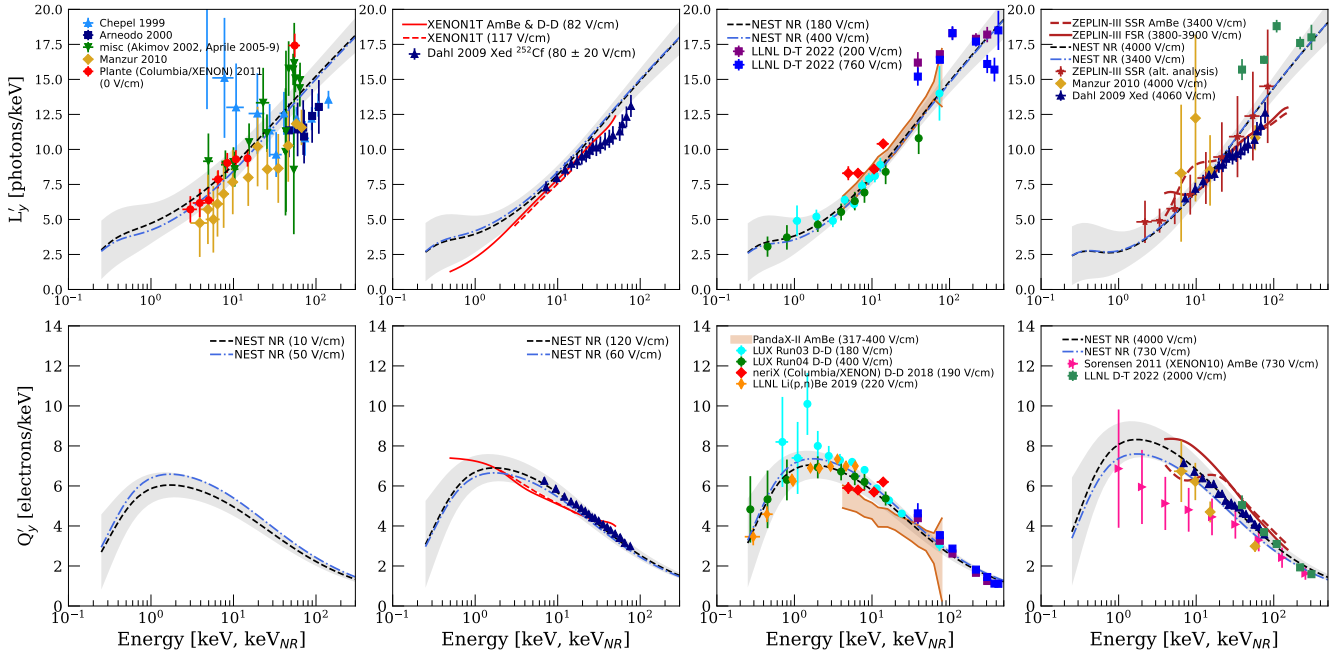


Figure 3. (NR) L'_y (top) and Q'_y (bottom) vs. E , from $\mathcal{E} = 0$ V/cm at left to the highest \mathcal{E} for which data exist at right [19, 20, 64, 65, 66, 67, 68, 69, 70, 71, 8, 72, 73, 74, 75, 76, 77, 78, 79]. Newer works from XENON1T and PandaX were not included in fits (yet agree at the $1-2\sigma$ level). NEST lines are blue and black, at similar \mathcal{E} s. Uncertainties on NEST increase as $E \rightarrow 0$ or ∞ , as the amount of data decreases at each extreme. \mathcal{E} dependence is weaker compared with ER (Figure 2). Summing L'_y and Q'_y results in a power law, not a constant (ER), while $N'_q < N_q$ [80, 15]. For systematically-offset data sets, our fit can average them if they share the same qualitative trend. Discrepant results sharing the same trend point towards a systematic offset in the S1 and/or S2 gains, with the S1 most affected by the 2-PE effect [81] and the S2 affected by assuming 100% e^- extraction prior to more recent measurements [82, 83]. Only Chepel 1999 L_y (upper left) is excluded from the fits used to tune NEST. As NR dE/dx decreases with decreasing E , e^- escape probability increases, causing L'_y to decrease. (L'_y 's shape is also determined by the \mathcal{L} -factor.) For Q'_y , there is a maximum, as the \mathcal{L} -factor decreases and $(1-r)$ increases as $E \rightarrow 0$, at different rates. In contrast to [15], where the focus was \mathcal{L} , we separate L'_y and Q'_y here. While errors imply no \mathcal{E} dependence, when data are taken in one detector at many \mathcal{E} s, a rising Q'_y (falling L'_y) with \mathcal{E} is clear [20].

2.3 Nuclear Recoils (Neutrons and WIMPs and Boron-8)

NR N'_q (differentiated in this section from ER with a prime) is well fit by a power law across >3 orders of magnitude in E (Fig. 5 within [15]). This is a simplification of the Lindhard approach to modeling the reduced quanta compared with ER, but also allows for departures from Lindhard at higher E s, lowering $N'_q(E)$'s rate of change with respect to Lindhard. Fewer equations and parameters are involved compared to Lindhard, which is a combination of multiple power laws inside of a rational function [84]: see Eqn. 8 in [15], where more justification is provided. NEST uses that simpler formula, repeated here:

$$N'_q = aE^b, \text{ where } a = 11^{+2.0}_{-0.5} \text{ and } b = 1.1 \pm 0.05. \quad (9)$$

The uncertainties here are $> 10\times$ those reported recently for the same fit, as only statistical error was included in Eqn. 6 of [15]. Here, systematic uncertainties in S1 detection efficiency and S2 gain (including e^- extraction efficiency) are included. They can be found inside the individual references in the Figure 3

caption. Individual power laws were found for each data set prior to the error-weighted combination, so that a data set with more points was not overly weighted. Equation 9 was also cross-checked with the L'_y and Q'_y individually extracted from data as displayed in Figure 3, and the raw S1 and S2 data of continuous energy spectrum sources.

Equation 9 can be used to define the “quenching,” \mathcal{L} :

$$\mathcal{L}(E, \rho) = N'_q(E) / N_q(E, \rho) = N'_q(E) W_q(\rho) / E, \quad (10)$$

interpreted as the fraction of total NR energy shared with the electron cloud to produce ions and excitons. \mathcal{L} permits one to define the electron equivalent energy in units of keV_{ee} for NR, as $\mathcal{L} \times (E \text{ in keV}_{nr})$, a best average reconstruction of the (combined-) E of recoiling nuclei. This \mathcal{L} should be applicable to neutron calibrations, WIMPs, and CE ν NS, such as from ^8B nuclear fusion [9].

While the previous equation set total quanta, the next equation determines the field- and density-dependent division into individual yields (charge or light) in an anti-correlated fashion, reducing r with higher field:

$$\varsigma(\mathcal{E}, \rho) = \gamma \mathcal{E}^\delta \left(\frac{\rho}{\rho_0} \right)^v, \text{ where } \gamma = 0.0480 \pm 0.0021 \text{ and } \delta = -0.0533 \pm 0.0068, \text{ and } v = 0.3. \quad (11)$$

The reference density $\rho_0 \equiv 2.90 \text{ g/cm}^3$. (The 2.89 value earlier was a very specific example, using LUX; the differences in yields are negligible.) The exponent v for the density dependence is hypothetical. It is not well measured at densities significantly deviating from ρ_0 [20].

We utilize Equation 11 to produce a Q'_y equation:

$$Q'_y(E, \mathcal{E}, \rho) = N_{e^-} \text{ per keV} = \frac{1}{\varsigma(\mathcal{E}, \rho)(E + \epsilon)^p} \left(1 - \frac{1}{1 + (\frac{E}{\zeta})^\eta} \right), \text{ where} \\ \epsilon = 12.6^{+3.4}_{-2.9} \text{ keV}, p = 0.5, \zeta = 0.3 \pm 0.1 \text{ keV}, \text{ and } \eta = 2 \pm 1. \quad (12)$$

Energy deposited is again E (in keV), and ϵ is the reshaping parameter for the E dependence. Higher or lower ς lowers or raises the Q'_y level respectively, providing the field-dependent shape of $Q'_y(E)$. ϵ can be thought of as the characteristic E where the Q'_y changes in its behavior from \sim constant at $O(1 \text{ keV})$ to falling at $O(10 \text{ keV})$. (Note ς has adaptable units of keV^{1-p} .)

ζ and η are the two sigmoid parameters that control the Q'_y roll-off at sub-keV energies. They permit a better match to not only the most recent calibrations [77, 73], but also to NEST versions pre-2.0, and other past models. Combining Thomas-Imel recombination with Lindhard (Eqn. 8 of [15]) produces a roll-off in Q'_y which is less steep than observed in data. Here, η controls steepness, allowing for an improved modeling of low-energy NR [45, 80], while ζ represents a characteristic scale for NR to ionize one e^- [15, 85]. At high E , $p = 0.5$ reproduces $Q'_y \propto 1/\sqrt{E}$ (Figure 3, bottom row).

Similar to ER, N_{ph} is derived from $N'_q - N_{e^-}$, but this is only a temporary anti-correlation enforcement; an additional sigmoid permits L'_y 's flexibility (Equation 13). Future calibration data could show a drop, or even flattening potentially, due to additional N_{ph} from the Migdal effect [72, 86]. An L'_y increase is possible even as $E \rightarrow 0$. This is not unphysical as long as N_{ph} vanishes in that limit, conserving E .

$$L_y'' = \frac{N_q'}{E} - Q_y', \quad N_{ph} = L_y'' E \left(1 - \frac{1}{1 + (\frac{E}{\theta})^\iota} \right); \quad L_y' = \frac{N_{ph}}{E},$$

$$\text{where } \theta = 0.3 \pm 0.05 \text{ keV and } \iota = 2 \pm 0.5. \quad N_q' = N_{ph} + N_{e-}. \quad (13)$$

The top row of Figure 3, especially if it is read from right to left, shows the same L_y' shape at all fields, indicative once again of a zero-field phantom Q_y' . In the L_y' calculation, L_y'' is a temporary variable (perfect anti-correlation) used within NEST to calculate the final L_y' and N_q' . The best-fit numbers for θ and ι match those of their counterparts ζ and η for Q_y' . In this modular but smooth approach the sigmoidal terms in L_y' and Q_y' go to 1.0 with increasing E . In this fashion it is possible to fit the low- and high- E regimes separately, allowing for a possibility that different physics occurs in the sub-keV region, by avoiding use of higher- E data to over-constrain lower- E yields.

The two sigmoids lower the predictive power of NEST for extrapolation into newer, lower- E regimes where no calibrations exist. In the case of L_y' , it will be challenging to achieve any with low uncertainty.

θ is a physically-motivated characteristic energy for release of a single (VUV) photon. Like ζ , its value is 300 eV, in agreement with Sorensen [85], and NEST pre-v2.0.0 [45]. Fundamental physics models for the \mathcal{L} governing total quanta, such as Lindhard [84] and Hitachi [87, 88], coupled to the Thomas-Imel “box” model for recombination [35], predict a similar value. Larger θ means more E is needed to produce a single photon (as opposed to excitons) and L_y' is lowered. This may potentially be detectable for an experiment with sufficient light collection efficiency.

Decreasing ι would lower L_y' as well, halving L_y' across all E when $\iota = 0$. On the other hand, in the limit of infinite ι (and/or $\theta \rightarrow 0$) the effect of the sigmoid is entirely removed, raising L_y' at low E . The same is true for η and ζ in the Q_y' formulation. A hard cut-off for any quanta was implemented in NEST for $E < W_q$ ($N_q / N_q' \approx 200$ eV). N_q represents the quanta which would have been generated for same- E ER. Below this, no quanta are generated. Sub-keV recoils have been observed at 200–400 V/cm (Figure 3).

In contrast to ER, for which the data suggest strict anti-correlation, simulated $\langle N_q' \rangle$ is not varied with a common Fano factor shared by both types of quanta for simplicity. For NR, there are (nominally) separate Fano factors for the excitation and ionization which can soften the strict anti-correlation at the level of the fundamental quanta. $\langle N_{ex} \rangle$ is smeared using a Gaussian of standard deviation $\sigma_{ex} = \sqrt{F_{ex} \langle N_{ex} \rangle}$. $\langle N_i \rangle$ is similarly varied, using $\sigma_i = \sqrt{F_i \langle N_i \rangle}$, as is standard practice for Fano factors [89]. Based upon the sparse existing reports of NR E resolution [72, 77, 90] both F_{ex} and F_i are set to 0.4 in NEST (as of v2.3.11; 1 earlier) though some data imply $F_{ex} \gg 1$ [72, 90]. $N_{ex} = G[\langle N_{ex} \rangle, \sigma_{ex}]$ and $N_i = G[\langle N_i \rangle, \sigma_i]$ (G =Gauss).

Using the same functional form as in Equation 8 from ER, NEST models fluctuations in recombination for redistribution of photons and electrons prior to measurable NR S1 and S2. The new parameters are distinguished using a prime superscript again for NR ($'$).

Parameter values are similar but not identical to those from ER: $A' = 0.04$ (as of v2.3.11 and fixed for all fields), $\xi' = 0.50$, and $\omega' = 0.19$ ($\alpha_p' = 0$). Over time, these do appear to have been converging upon values similar to ER's. These set a final recombination width σ_r' . N_{e-} and N_{ph} distributions have that width but are skewed due to NR recombination asymmetry ($\alpha_r' = 2.25$). α_r' may be higher, but it is difficult to disambiguate NR skew (less L_y) in data from unresolved multiple scatters, other detector effects [59], or Migdal-Effect ER, which can raise Q_y and generate a secondary population [91].

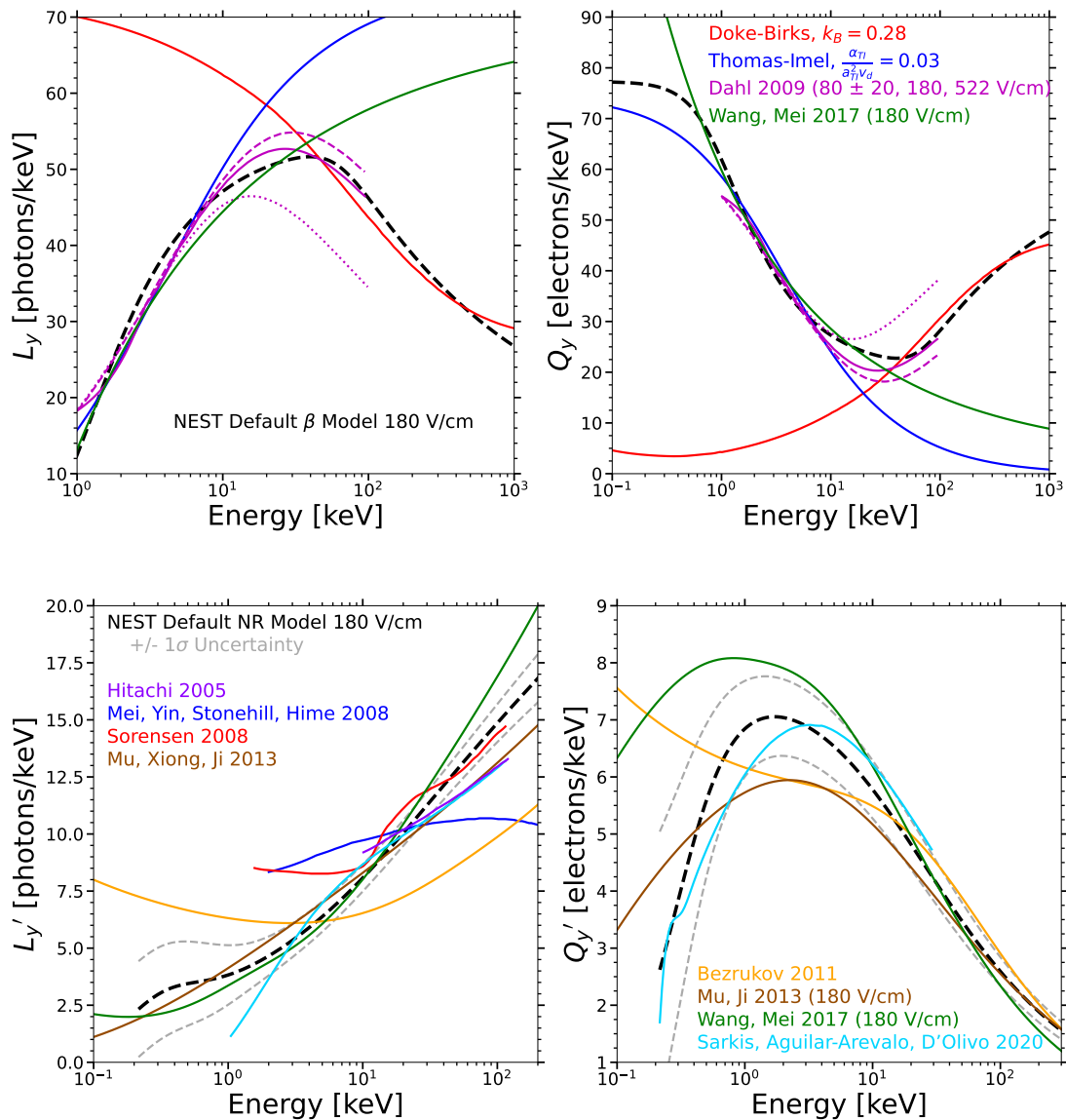


Figure 4. Comparing NEST with other approaches: L_y (left) and Q_y (right) alternate, for ER (top) and NR (bottom), at 180 V/cm [18, 35, 20, 92]. The right legends apply to both the left and right plots. This was LUX's initial field [93], in between XENON1T at 80 [94] and earlier works like [44] as high as 730 V/cm. While similar to fundamental approaches, NEST incorporates features of multiple, splitting differences and following the data. The Thomas-Imel (T-I) and Doke / Birks sample curves shown are meant to match 180 V/cm the most closely. Unlike the T-I and plasma models, NEST accounts for the high- E (low- dE/dx) L_y decrease (Q_y increase) [92]. Birks' Law does too, but fails to work at low E s (high dE/dx) [95]. Dahl presented variations on T-I, utilizable for high E s by breaking up tracks into boxes, although his closest fields were 80 and 522 V/cm [20]. We show a 180 V/cm model (solid), *i.e.*, the weighted average of his 80 (dashed) and 522 V/cm (dotted) models. There are more NR models (right), due to a need to explain potential WIMPs [92, 87, 96, 97, 98, 99, 100, 101]. Older models based on L_{eff} , which was L'_y relative to ^{57}Co γ -rays (122 keV), were translated assuming 64 photons/keV at 0 V/cm with a small error [14, 102], unless papers had a different value, which we then used instead (Bezrukov: 53). If they presented multiple models, we plot the most central one and/or one closest to data. Comparisons are only qualitative here, ensuring NEST has the correct, physically-motivated shape across different regimes.

3 COMPARISONS TO FIRST-PRINCIPLES APPROACHES

By smoothly interpolating data sets taken at individual energies and/or electric fields NEST is now fully empirical, built upon sigmoids and power laws as needed for a continuous model. But inherent uncertainty is introduced by extrapolating into new energy and/or field regimes. To assess that, and to further validate an empirical approach, we show agreement with the models closer to “first principles.” Within NEST’s earliest versions, the Thomas-Imel (T-I) box model [35] was used for low energy, while Birks’ Law of scintillation was adapted for high energy. Both were qualitatively explained in Section 2.1, but are quantified here. The latter approach inside NEST was similar to Doke’s modification [14] for scintillation alone, but applied to recombination directly so it can model both the L_y and the Q_y :

$$\langle r \rangle = \frac{k_A \frac{dE}{dx}}{1 + k_B \frac{dE}{dx}} + k_C, \text{ with } k_C = 1 - k_A/k_B. \quad (14)$$

This is Birks’ Law for other scintillators [95] but with an additional constant k_C that accounts for parent-ion recombination [18]. Its constraint ensures $\langle r \rangle$ is between 0–1, as it is a probability. A best fit to ER (γ) data has a non-zero k_C only at 0 V/cm; at non-zero \mathcal{E} , Equation 14 contains only one Birks’ constant, $k_A = k_B$.

k_B ’s best-fit value (for 180 V/cm) is 0.28, from a fit to only the high- E portion of the NEST β ER model. That is in turn supported by ^3H , ^{14}C , and ^{220}Rn data from LUX and XENON. Notably, k_B in NEST v0.9x and the first NEST paper 13 years ago for this \mathcal{E} was 0.257, within 10% of the value in Figure 4 (upper right plot pane), which covers many alternative approaches to NEST.

Despite Birks’ great success in explaining data at high E , that model cannot capture the behavior of ER at $E \lesssim 50$ keV. While lower- E extensions are possible, such as addition of higher-order terms in dE/dx for that region, we instead consider the T-I model for lower E :

$$\langle r \rangle = 1 - \frac{\ln(1 + \xi_{TI})}{\xi_{TI}}, \text{ where } \xi_{TI} = \frac{N_i}{4} \frac{\alpha_{TI}}{a_{TI}^2 v_d}. \quad (15)$$

ξ_{TI} parameterizes the physical principles. α_{TI} describes diffusion, v_d is e^- drift velocity, and N_i is again number of ions. Diffusion is modeled by using the relation $\alpha_{TI} = De^2/(kT\epsilon_d)$, where D combines e^- and positive-ion diffusion coefficients, e is the elementary charge, k is Boltzmann not Birks, T is temperature, and $\epsilon_d = 1.85 \times \epsilon_0$ is the dielectric constant. $D = 18.3 \text{ cm}^2/\text{s}$ is the longitudinal diffusion constant for e^- s at 180 V/cm, derived from S2 pulse lengths [103]. e^- diffusion dominates over cation diffusion. Assuming this D (and the $T = 173$ K from earlier), as well as ϵ_d as defined above, and taking $v_d = 1.51 \text{ mm}/\mu\text{s}$ at field $\mathcal{E} = 180 \text{ V/cm}$ [104], we find $\alpha_{TI} = 1.20 \times 10^{-9} \text{ m}^3/\text{s}$. From this, the escape probability ($1 - \langle r \rangle$) for electrons inside a box is found by solving the relevant (Jaffé) differential equations (please see Section 6.2 of [20] for the details).

We interpret a_{TI} , the size of the “box” surrounding ionized atoms, as corresponding to a (\mathcal{E} -independent) e^- -ion thermalization distance of $4.6 \mu\text{m}$, as calculated by Mozumder [105]. This value was used before as a border in NEST for track length, to switch from T-I to Birks. The ultimate value of $\text{TIB} \equiv \alpha_{TI}/(a_{TI}^2 v_d)$ for that case is 0.0376.

Dahl found best-fit values of TIB ranging from 0.03–0.04 for both ER and NR data at 60–522 V/cm [20]. Our contemporary fits (for NEST and for data), the blue lines at low energies in the first two panels at top in Figure 4, used 0.0300. If v_d changes with drift field (it is typically $O(2 \text{ mm}/\mu\text{s})$ [106]), then the entire ranges of Dahl, and of Sorensen and Dahl, are covered: 0.02–0.05 [80].

For NR, one sees in Figure 4 (bottom row) many different past models, mainly for L_y . NEST originally used T-I for NR, as Dahl / Sorensen [20, 80]. See the blue lines in Figure 5. It applies the same color convention as Figure 4. While T-I fixes r , thus partitioning E into L_y vs. Q_y , the total yield must still be determined. For the maximal distinction, we have selected the original Lindhard formula for that, as laid out in multiple other works [84, 80, 72, 15], not Equation 9. We set the crucial Lindhard parameter $k_L = 0.166$, the decades-old default for Xe [84]. Averaging over E , $N'_q/N_q \approx k_L \cdot 0.166$ is consistent with actual data [72], Lenardo's meta-analysis [102], and NEST v2.3+.

We identify ς of Equation 12 with TIB value, as justified by Equation 11, wherein the parameters for the \mathcal{E} dependence of ς (γ and δ) overlap at the 1σ level with the power-law field dependence of TIB from [102]. At 180 V/cm, $\varsigma = 0.0362$, quite close to our theoretical calculation earlier and comparable to a best-fit TIB for ER. $N_{ex}/N_i = 1.0$ is assumed. While higher than for ER, it is the most common assumption for NR, and best fits to data and theory vary from 0.7–1.1 [80].

An additional quenching is applied to just L'_y [69]. We find a common parameterization of this effect [99] to be defined in a manner analogous to Birks' Law or Equation 14:

$$q = \frac{1}{1 + \kappa \epsilon_Z^\lambda}, \text{ with } \epsilon_Z \approx 10^{-3} E, \quad (16)$$

where $q < 1$ is a multiplicative factor on L'_y . ϵ_Z is unitless reduced energy, useful for comparison between elements. Equation 16 is like 14. The power law can be identified as proportional to NR dE/dx . If we define dE/dx (or LET) as approximately $\beta' \epsilon^\lambda$, then $\kappa = k_B \beta' \mathcal{L}$. Assuming the ER k_B (defined as 0.28 for 180 V/cm in Figure 4 top), $\mathcal{L} \sim 0.15$ (11/73) per an energy-independent approximation of Equation 9 justified by the power being close to 1, and $\beta' = 100$, then $\kappa = 4.20$, $< 0.2\sigma$ away from [102]. A fraction of the quanta removed from L'_y in 16 may be convertible into Q'_y . Figure 5 right explores that with the fraction as 0.1.

Unlike with ER, Birks' Law models NR over the entire E range of interest (Figure 5, red) with $k_B = 0.28$ and $dE/dx = \beta' \epsilon^\lambda = 100\epsilon$. While there is disagreement about whether λ is 1.0 or 0.5 depending on the E regime [87, 88], 1.0 only differs by 1.6σ from the value of 1.14 in [102].

Looking back at alternatives to Lindhard, in Figure 4, we see NEST's power law, L'_y , and Q'_y seem a good match for Mu and Xiong [98, 100], also for Wang and Mei [92, 96]. NEST's lower 1σ line touches Sarkis' L'_y [101], which is low due to not including the most recent points [72, 75]. On the high- E L'_y end, NEST's upper uncertainty band encompasses neriX [76]. As for Q'_y , NEST lies in between [92] above and [100] and [101] below, falling in between LUX D–D [72] and LLNL [77].

The good agreement between the fully empirical NEST model and the first-principle models of both NR and ER shown here shows that NEST can accurately simulate potential dark matter signals and backgrounds, respectively. This should be the case even for the regimes where data are still lacking, or they exist but have large uncertainties. In the case of NR, the fully empirical approach reproduces all data better using a comparable number of free parameters, but much greater flexibility compared to semi-empirical approaches. For fluctuations, the number of NEST free parameters increased to two Fano factors (excitation, ionization) and four numbers for recombination width and skew, to fully model the E resolution. NEST, justified first using data, is not limited to the operating conditions of previous experiments to make predictions relevant for a future experiment, though L_y and Q_y must pass through a detector simulation to obtain realistic S1 and S2 pulse areas: the processes in Section 2.2.5 here and Appendix A of [107].

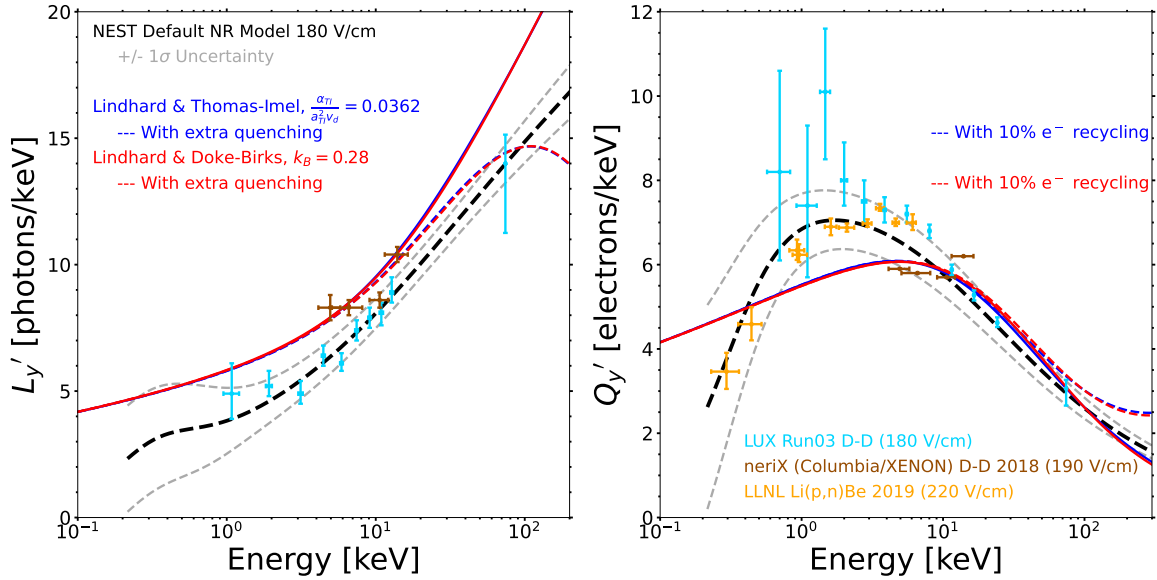


Figure 5. The comparisons of NEST and selected NR data to only the Thomas-Imel box (blue) and Birks (red) models of recombination, always using Lindhard here to define N'_q (found as Eqn. 8 in [15] and elsewhere). For L'_y , the dashed lines indicate additional quenching at higher E s and dE/dx , while for the Q'_y , where this quenching has no direct impact, the dotted lines indicate partial conversion of photons into e^- s from that effect (or not, solid lines). Some data, including at other fields, are consistent at a 1–2 σ level with no quenching or conversion, not the amounts shown. The L'_y data from 50–100 keV $_{nr}$ are inconsistent: see Figure 3 upper left and [70].

4 DISCUSSION AND FUTURE WORK

Beginning with our models of beta ER, gamma-ray ER, and the NR light and charge yields, along with resolution modeling, a coherent picture was built up inside of the NEST framework, which enables a good agreement with data. NEST was also shown to have features from multiple first-principles approaches, such as the box and Birks models. NEST already works for LAr [15] using the same formulae as LXe but unique parameter values. However, it still works best only for point-like interactions, like those in dark matter experiments like DarkSide, not tracks, as will be observed by DUNE. The list of NEST collaborators includes TESSERACT [108] members, so addition of liquid helium (LHe) to NEST is planned.

Looking beyond LHe, short-term future work includes a NEST re-writing to account for the lower W_q measured by EXO and Baudis et al. [46, 109], but this will be easier if NEST can return to approaches closer to first principles. Therefore, there will also be a concerted effort made to return to a semi-empirical formulation by application of a modified T-I model pioneered by ArgoNeuT [110], combined with a literal breakup of long tracks into boxes as done in the thesis of Dahl, allowing higher energies to exhibit lower light yields without hard-coding that, by virtue of being comprised of multiple, lower- E interaction sites. High- E modeling is thus accomplished by having one model for all E s, but treating high- E interactions as series of many low- E fragments wherein the L_y will continue to be monotonically increasing with E . The main motivation for this is greater confidence in extrapolations to uncalibrated regions of future detectors.

The modified box model of LArTPC-based high- E neutrino experiments should also be useful for LXe NR. We demonstrate now how it represents a more generalized version of the current NR model:

$$Q'_y = \frac{N_{e^-}}{E} = (1 - r) \frac{N_i}{E} = \frac{\ln(a' + \xi)}{\xi} \frac{N_i}{E} = \frac{\ln(a' + \xi)}{\xi} \frac{N_q/E}{1 + \alpha_x} = \frac{\ln(a' + \xi)}{\xi E} \frac{aE^b}{1 + \alpha_x}, \quad (17)$$

where $a' \equiv 1$ in default T-I (but relaxing this constraint to $O(1)$ as per [110] can better fit data), ξ is short for ξ_{TI} , redefined as $\beta dE/dx$ with β as a constant (not Equation 15), and $\alpha_x \equiv N_{ex}/N_i$ for conciseness.

$$Q'_y = \frac{aE^{b-1} \ln(1 + \beta \frac{dE}{dx})}{1 + \alpha_x \beta \frac{dE}{dx}} \approx \frac{a}{1 + \alpha_x} \frac{\ln(1 + \beta \frac{dE}{dx})}{\beta \frac{dE}{dx}} \approx \frac{a \ln(1 + \beta \frac{dE}{dx})}{2 \beta \frac{dE}{dx}} \approx 5 \frac{\ln(1 + \beta \frac{dE}{dx})}{\beta \frac{dE}{dx}}, \quad (18)$$

where we employ, in order, the approximations $b \approx 1$, $\alpha_x \approx 1$, and $a \approx 10$ (Equation 9). Fitting to the SRIM line in Fig. 5 of [88] one finds for NR, in normalized (dimensionless) units, that stopping power is:

$$dE/dx = \beta' \epsilon_Z^{0.5} = 120 \sqrt{\epsilon_Z} = 120 \sqrt{0.001E} = 120 \sqrt{0.001} \sqrt{E} = 3.8 \sqrt{E}, \quad (19)$$

valid for the range of 0–100 keV. However, near 50 keV, a square root function with an offset fits nearly as well to SRIM: $3.4 \sqrt{E + \epsilon}$, with $\epsilon = 12.6$ keV (Equation 12). Making the ansatz $\beta \sim \varsigma$ (Equation 11),

$$Q'_y \approx 5 \frac{\ln(1 + \varsigma \frac{dE}{dx})}{\varsigma \frac{dE}{dx}} = 5 \frac{\ln(1 + 0.036 \cdot 3.4 \sqrt{E + 12.6})}{0.036 \cdot 3.4 \sqrt{E + 12.6}} = \frac{5 \cdot 0.677}{3.4 \varsigma \sqrt{E + \epsilon}} = \frac{1}{\varsigma \sqrt{E + \epsilon}}, \quad (20)$$

recovering the high- E portion of Equation 12 at $\varsigma = 0.036$ (200 V/cm) and $E = 50$ keV. By modifying the power law for N_q to be $aE^b - C$ [111], it may be possible to eliminate the need for the sigmoids for reducing both Q_y and L_y at the lowest E s, combining C with an additional degree of freedom, a non-unity a' in the natural log. By replacing our present equation (12 or 20) with Equation 17 we should be able to find a sufficiently-flexible compromise that fits data with the same number of free parameters, or fewer even (eliminating the sigmoid roll-offs, as well as the ϵ offset in dE/dx potentially) all motivated from first principles (T-I). The redefinition of ξ_{TI} in terms of dE/dx permits a non-linearity in the dependence of ξ on N_i and an incorporation of dE/dx (as in the Doke / Birks' Law), while α_x could be made E and \mathcal{E} -dependent as in Eq. (B8) of [62], if absolutely necessary, following the similar increase with E for ER in Equation 2 (mimicked by Eq. (A4)'s exponential in [62]). Lastly, the replacement of $aE^b - C$ with E/W_q in Equation 17 could permit usage for ER, as in LAr, from the keV to the GeV scales.

Improved modeling of the MeV (ERs) scale is important for searches for neutrinoless double-beta ($0\nu\beta\beta$) decay, for which the key discrimination is not NR vs. ER, but between two forms of the latter (β vs. γ). EXO-200 [3] and KamLAND-Zen [112] have produced the two most stringent half-life limits for ^{136}Xe , and are highly competitive with the Ge-based experiments. In addition to these results, one must evaluate the prospects of nEXO [113], as well as of LZ [114], XENONnT [115], and XLZD [116] for this field of nuclear physics. The dark-matter-focused experiments have greater ER backgrounds compared to nEXO, but superior energy resolution.

Longer-term future work on NEST will involve an *ab initio* MC with cross sections for recombination and the other processes [117], and/or molecular dynamics modeling of Xe atoms with the 12-6 Lennard-Jones potential for van der Waals forces. LXe values are known, for L-J (and more advanced models [118]):

$$V(d) = 4\epsilon_{LJ} \left[\left(\frac{R}{d} \right)^{12} - \left(\frac{R}{d} \right)^6 \right], \text{ where } \epsilon_{LJ} = 1.77 \text{ kJ/mol and } R = 4.10 \text{ \AA} \quad (21)$$

While these approaches are challenging for high (MeV) energies, at sub-keV scales where yields are more uncertain, *e.g.* for ^8B , fewer interactions are involved, leading to a more computationally tractable problem.

CONFLICT OF INTEREST STATEMENT

All of the authors declare that the research was conducted in the absence of any commercial or financial relationships that could be construed as a potential conflict of interest.

AUTHOR CONTRIBUTIONS

MS and GRCR did most of the writing and are responsible for the majority of plots and analyses. JB forged the original beta models; GAB worked on ER energy reconstruction; JPB debugged code; EB, ACK, and DNM read and revised text; JEC and ESK improved the functionality of the NEST code and contributed to multiple unique analyses; SJF and CSL created Figures 1–3 together; JH and ZZ worked on the gamma model; KM researched the work function discrepancy; RM, KT, and MDW worked on the NR models; MM, JM, and SW provided an outside perspective, from the LAr communities; KN and CDT represented the XENON collaboration's points of view; MT hosted the NEST website at his institution (UCD); VV read the text and revised it extensively, in addition to being responsible for Figures 4 and 5. MZ looked at the field dependence of the ER and NR yields.

FUNDING

This work was supported by the U.S. Department of Energy (DOE) under Awards DE-SC0015535, DE-SC0024225, DE-SC0021388, DE-SC0018982 and DE-AC02-05CH11231, and by the National Science Foundation (NSF) under Awards 2046549 and 2112802.

ACKNOWLEDGMENTS

We thank the LZ/LUX plus XENON1T/nT/DARWIN collaborations for useful recent discussion as well as continued support for NEST work. We especially thank LUX for providing key detector parameters, and LUX collaborator Prof. Rick Gaitskell (of Brown University), Dr. Xin Xiang (formerly of Brown, now at Brookhaven National Laboratory), and Dr. Quentin Riffard (Lawrence Berkeley National Laboratory), for critical discussions regarding the detector performance of a potential Generation-3 liquid Xe TPC detector.

SUPPLEMENTAL DATA

Please see Appendices A and B.

DATA AVAILABILITY STATEMENT

The data presented in this study are available upon request.

REFERENCES

- 1 .Baudis L. The search for dark matter. *European Review (Cambridge University Press)* **26** (2018) 70–81. doi:10.1017/S1062798717000783.
- 2 .Akerib DS, et al. An effective field theory analysis of the first LUX dark matter search. *Phys. Rev. D* **103** (2021) 122005. doi:10.1103/PhysRevD.103.122005.
- 3 .Anton G, et al. Search for Neutrinoless Double- β Decay with the Complete EXO-200 Dataset. *Phys. Rev. Lett.* **123** (2019) 161802. doi:10.1103/PhysRevLett.123.161802.

- 4 .Aprile E, et al. Observation of two-neutrino double electron capture in ^{124}Xe with XENON1T. *Nature* **568** (2019) 532–535. doi:10.1038/s41586-019-1124-4.
- 5 .Aprile E, et al. First Measurement of Solar ^8B Neutrinos via Coherent Elastic Neutrino-Nucleus Scattering with XENONnT. *arXiv:2408.02877* (2024).
- 6 .Bo Z, et al. First Indication of Solar ^8B Neutrino Flux through Coherent Elastic Neutrino-Nucleus Scattering in PandaX-4T. *arXiv:2407.10892* (2024).
- 7 .Akerib DS, et al. Simulations of Events for the LUX-ZEPLIN (LZ) Dark Matter Experiment. *Astroparticle Physics* **125** (2021) 102480. doi:10.1016/j.astropartphys.2020.102480.
- 8 .Yan B, et al. Determination of responses of liquid xenon to low energy electron and nuclear recoils using a PandaX-II detector. *Chinese Physics C* **45** (2021) 075001. doi:10.1088/1674-1137/abf6c2.
- 9 .Aprile E, et al. Search for Coherent Elastic Scattering of Solar ^8B Neutrinos in the XENON1T Dark Matter Experiment. *Phys. Rev. Lett.* **126** (2021) 091301. doi:10.1103/PhysRevLett.126.091301.
- 10 .Caratelli D, et al. Low-Energy Physics in Neutrino LArTPCs. *arXiv:2203.00740* (2022).
- 11 .Abud AA, et al. Identification and reconstruction of low-energy electrons in the ProtoDUNE-SP detector. *Phys. Rev. D* **107** (2023) 092012. doi:10.1103/PhysRevD.107.092012.
- 12 .Westerdale S. The DEAP-3600 liquid argon optical model and NEST updates. *JINST* **19** (2024) C02008. doi:10.1088/1748-0221/19/02/C02008.
- 13 .Aalbers J, et al. First Dark Matter Search Results from the LUX-ZEPLIN (LZ) Experiment. *Physical Review Letters* **131** (2023). doi:10.1103/physrevlett.131.041002.
- 14 .Szydajis M, Barry N, Kazkaz K, Mock J, Stolp D, Sweany M, et al. NEST: A Comprehensive Model for Scintillation Yield in Liquid Xenon. *JINST* **6** (2011) P10002.
- 15 .Szydajis M, Block GA, Farquhar C, Flesher AJ, Kozlova ES, Levy C, et al. A Review of Basic Energy Reconstruction Techniques in Liquid Xenon and Argon Detectors for Dark Matter and Neutrino Physics Using NEST. *Instruments* **5** (2021) 13. doi:10.3390/instruments5010013.
- 16 .Aprile E, Budnik R, Choi B, Contreras HA, Giboni KL, Goetzke LW, et al. Measurement of the scintillation yield of low-energy electrons in liquid xenon. *Phys. Rev. D* **86** (2012) 112004. doi:10.1103/PhysRevD.86.112004.
- 17 .Baudis L, Dujmovic H, Geis C, James A, Kish A, Manalaysay A, et al. Response of liquid xenon to Compton electrons down to 1.5 keV. *Phys. Rev. D* **87** (2013) 115015.
- 18 .Doke T, Hitachi A, Kikuchi J, Masuda K, Okada H, Shibamura E. Absolute scintillation yields in liquid argon and xenon for various particles. *Japanese Journal of Applied Physics* **41** (2002) 1538–1545. doi:10.1143/jjap.41.1538.
- 19 .Aprile E, et al. XENON1T dark matter data analysis: Signal and background models and statistical inference. *Phys. Rev. D* **99** (2019) 112009. doi:10.1103/PhysRevD.99.112009.
- 20 .Dahl CE. *The physics of background discrimination in liquid xenon, and first results from XENON10 in the hunt for WIMP dark matter*. Ph.D. thesis, Princeton University (2009).
- 21 .Boulton EM, et al. Calibration of a two-phase xenon time projection chamber with a ^{37}Ar source. *JINST* **12** (2017) P08004. doi:10.1088/1748-0221/12/08/P08004.
- 22 .Akerib D, et al. Improved Measurements of the β -Decay Response of Liquid Xenon with the LUX Detector. *Phys. Rev. D* **100** (2019) 022002. doi:10.1103/PhysRevD.100.022002.
- 23 .Aprile E, et al. Signal yields of keV electronic recoils and their discrimination from nuclear recoils in liquid xenon. *Phys. Rev. D* **97** (2018) 092007. doi:10.1103/PhysRevD.97.092007.
- 24 .Akerib DS, et al. Ultra-low energy calibration of LUX detector using ^{127}Xe electron capture. *Phys. Rev. D* **96** (2017) 112011. doi:10.1103/PhysRevD.96.112011.

- 25 .Goetzke L, Aprile E, Anthony M, Plante G, Weber M. Measurement of light and charge yield of low-energy electronic recoils in liquid xenon. *Phys. Rev. D* **96** (2017) 103007.
- 26 .Akimov D, et al. Experimental study of ionization yield of liquid xenon for electron recoils in the energy range 2.8–80 keV. *JINST* **9** (2014) P11014. doi:10.1088/1748-0221/9/11/p11014.
- 27 .Akerib DS, et al. Improved modeling of beta electronic recoils in liquid xenon using LUX calibration data. *Journal of Instrumentation* **15** (2020) T02007. doi:10.1088/1748-0221/15/02/t02007.
- 28 .[Dataset] Szydagis M, et al. NEST: Noble Element Simulation Technique, A Symphony of Scintillation <http://nest.physics.ucdavis.edu> (2020).
- 29 .Conti E, DeVoe R, Gratta G, Koffas T, Waldman S, Wodin J, et al. Correlated fluctuations between luminescence and ionization in liquid xenon. *Phys. Rev. B* **68** (2003) 054201. doi:10.1103/PhysRevB.68.054201.
- 30 .Bressi G, Carugno G, Conti E, Noce C, Iannuzzi D. Infrared scintillation: a comparison between gaseous and liquid xenon. *Nuclear Instruments and Methods in Physics Research Section A: Accelerators, Spectrometers, Detectors and Associated Equipment* **461** (2001) 378–380. doi:https://doi.org/10.1016/S0168-9002(00)01249-3. 8th Pisa Meeting on Advanced Detectors.
- 31 .Aprile E, Bolotnikov AE, Bolozdynya AL, Doke T. *Noble Gas Detectors* (Wiley) (2008). doi:10.1002/9783527610020.
- 32 .Szydagis M, Levy C, Blockinger G, Kamaha A, Parveen N, Rischbieter G. Investigating the XENON1T Low-Energy Electronic Recoil Excess Using NEST. *Phys. Rev. D* **103** (2021) 012002. doi:10.1103/PhysRevD.103.012002.
- 33 .Akerib DS, et al. Tritium calibration of the LUX dark matter experiment. *Phys. Rev. D* **93** (2016) 072009.
- 34 .Lin Q, Fei J, Gao F, Hu J, Wei Y, Xiao X, et al. Scintillation and ionization responses of liquid xenon to low energy electronic and nuclear recoils at drift fields from 236 V/cm to 3.93 kV/cm. *Phys. Rev. D* **92** (2015) 032005. doi:10.1103/PhysRevD.92.032005.
- 35 .Thomas J, Imel DA. Recombination of electron-ion pairs in liquid argon and liquid xenon. *Phys. Rev. A* **36** (1987) 614–616. doi:10.1103/PhysRevA.36.614.
- 36 .Doke T, Crawford HJ, Hitachi A, Kikuchi J, Lindstrom PJ, Masuda K, et al. LET dependence of scintillation yields in liquid argon. *Nuclear Instruments and Methods in Physics Research Section A: Accelerators, Spectrometers, Detectors and Associated Equipment* **269** (1988) 291–296. doi:https://doi.org/10.1016/0168-9002(88)90892-3.
- 37 .[Dataset] Szydagis M, et al. Noble Element Simulation Technique (2022). doi:10.5281/zenodo.6989015.
- 38 .[Dataset] Berger M, Coursey J, Zucker M, Chang J. ESTAR, PSTAR, and ASTAR: Computer Programs for Calculating Stopping-Power and Range Tables for Electrons, Protons, and Helium Ions (National Institute of Standards and Technology, Gaithersburg, MD 2005).
- 39 .Obodovskii I, Ospanov K. Scintillation output of liquid xenon for low-energy gamma-quanta. *Instruments and Experimental Techniques* **37** (1994) 42–45.
- 40 .Yamashita M, Doke T, Kawasaki K, Kikuchi J, Suzuki S. Scintillation response of liquid Xe surrounded by PTFE reflector for gamma rays. *Nuclear Instruments and Methods in Physics Research Section A: Accelerators, Spectrometers, Detectors and Associated Equipment* **535** (2004) 692–698. doi:https://doi.org/10.1016/j.nima.2004.06.168.
- 41 .Akerib DS, et al. Signal yields, energy resolution, and recombination fluctuations in liquid xenon. *Phys. Rev. D* **95** (2017) 012008. doi:10.1103/PhysRevD.95.012008.

- 42 .Tan A, et al. Dark Matter Results from First 98.7 Days of Data from the PandaX-II Experiment. *Phys. Rev. Lett.* **117** (2016) 121303. doi:10.1103/PhysRevLett.117.121303.
- 43 .Aprile E, et al. First Dark Matter Results from the XENON100 Experiment. *Phys. Rev. Lett.* **105** (2010) 131302. doi:10.1103/PhysRevLett.105.131302.
- 44 .E Aprile *et al.* Design and performance of the XENON10 dark matter experiment. *Astroparticle Physics* **34** (2011) 679 – 698. doi:https://doi.org/10.1016/j.astropartphys.2011.01.006.
- 45 .Szydajis M, Fyhrie A, Thorngren D, Tripathi M. Enhancement of NEST Capabilities for Simulating Low-Energy Recoils in Liquid Xenon. *JINST* **8** (2013) C10003. doi:10.1088/1748-0221/8/10/C10003.
- 46 .Anton G, et al. Measurement of the scintillation and ionization response of liquid xenon at MeV energies in the EXO-200 experiment. *Phys. Rev. C* **101** (2020) 065501. doi:10.1103/PhysRevC.101.065501.
- 47 .Doke T, Hitachi A, Kubota S, Nakamoto A, Takahashi T. Estimation of Fano factors in liquid argon, krypton, xenon and xenon-doped liquid argon. *Nuclear Instruments and Methods* **134** (1976) 353 – 357. doi:https://doi.org/10.1016/0029-554X(76)90292-5.
- 48 .Alvarez V, et al. Near-Intrinsic Energy Resolution for 30 to 662 keV Gamma Rays in a High Pressure Xenon Electroluminescent TPC. *Nucl. Instrum. Meth. A* **708** (2013) 101–114. doi:10.1016/j.nima.2012.12.123.
- 49 .Delaquis S, et al. Deep neural networks for energy and position reconstruction in EXO-200. *Journal of Instrumentation* **13** (2018) P08023. doi:10.1088/1748-0221/13/08/p08023.
- 50 .Aprile E, et al. Energy resolution and linearity of XENON1T in the MeV energy range. *The European Physical Journal C* **80** (2020) 8. doi:10.1140/epjc/s10052-020-8284-0.
- 51 .Aprile E, Giboni KL, Majewski P, Ni K, Yamashita M. Observation of anticorrelation between scintillation and ionization for MeV gamma rays in liquid xenon. *Phys. Rev. B* **76** (2007) 014115. doi:10.1103/PhysRevB.76.014115.
- 52 .Aprile E, Mukherjee R, Suzuki M. Performance of a liquid xenon ionization chamber irradiated with electrons and gamma-rays. *Nuclear Instruments and Methods in Physics Research Section A: Accelerators, Spectrometers, Detectors and Associated Equipment* **302** (1991) 177 – 185. doi:https://doi.org/10.1016/0168-9002(91)90507-M.
- 53 .Platzman RL. Total ionization in gases by high-energy particles. *International Journal of Applied Radiation and Isotopes* **10** (1961) 116–127.
- 54 .Dobi A. *Measurement of the Electron Recoil Band of the LUX Dark Matter Detector With a Tritium Calibration Source*. Ph.D. thesis, Maryland U., College Park (2014). doi:10.13016/M24P5P.
- 55 .Amoruso S, et al. Study of electron recombination in liquid argon with the ICARUS TPC. *Nuclear Instruments and Methods in Physics Research Section A: Accelerators, Spectrometers, Detectors and Associated Equipment* **523** (2004) 275 – 286. doi:https://doi.org/10.1016/j.nima.2003.11.423.
- 56 .Thomas J, Imel DA, Biller S. Statistics of charge collection in liquid argon and liquid xenon. *Phys. Rev. A* **38** (1988) 5793–5800. doi:10.1103/PhysRevA.38.5793.
- 57 .Nygren DR. Columnar recombination: a tool for nuclear recoil directional sensitivity in a xenon-based direct detection WIMP search. *Journal of Physics: Conference Series* **460** (2013) 012006. doi:10.1088/1742-6596/460/1/012006.
- 58 .Davis C, et al. An Optimal Energy Estimator to Reduce Correlated Noise for the EXO-200 Light Readout. *JINST* **11** (2016) P07015. doi:10.1088/1748-0221/11/07/P07015.
- 59 .Akerib DS, et al. Discrimination of electronic recoils from nuclear recoils in two-phase xenon time projection chambers. *Phys. Rev. D* **102** (2020) 112002. doi:10.1103/PhysRevD.102.112002.

- 60 .Rischbieter GRC. *Signal Yields and Detector Modeling in Xenon Time Projection Chambers, and Results of an Effective Field Theory Dark Matter Search Using LUX Data*. Ph.D. thesis, UAlbany SUNY (2022).
- 61 .Aalbers J, et al. First Constraints on WIMP-Nucleon Effective Field Theory Couplings in an Extended Energy Region From LUX-ZEPLIN. *Physical Review D* **109** (2024). doi:10.1103/physrevd.109.092003.
- 62 .[Dataset] Aprile E, et al. XENONnT WIMP Search: Signal & Background Modeling and Statistical Inference (2024).
- 63 .Chepel V, Araújo H. Liquid noble gas detectors for low energy particle physics. *Journal of Instrumentation* **8** (2013) R04001. doi:10.1088/1748-0221/8/04/r04001.
- 64 .Chepel VY, et al. Primary scintillation yield and alpha/beta ratio in liquid xenon. *Proceedings of the 1999 IEEE 13th International Conference on Dielectric Liquids* (1999) 52.
- 65 .Arneodo F, et al. Scintillation efficiency of nuclear recoil in liquid xenon. *Nucl. Inst. and Meth. A* **449** (2000) 147.
- 66 .Akimov D, et al. Measurements of scintillation efficiency and pulse shape for low energy recoils in liquid xenon. *Phys. Lett. B* **524** (2002) 245–251.
- 67 .Aprile E, et al. Scintillation response of liquid xenon to low energy nuclear recoils. *Phys. Rev. D* **72** (2005) 072006.
- 68 .Aprile E, Baudis L, Choi B, Giboni KL, Lim K, Manalaysay A, et al. New measurement of the relative scintillation efficiency of xenon nuclear recoils below 10 keV. *Phys. Rev. C* **79** (2009) 045807. doi:10.1103/PhysRevC.79.045807.
- 69 .Manzur A, Curioni A, Kastens L, McKinsey D, Ni K, Wongjirad T. Scintillation efficiency and ionization yield of liquid xenon for mono-energetic nuclear recoils down to 4 keV. *Phys. Rev. C* **81** (2010) 025808. doi:10.1103/PhysRevC.81.025808.
- 70 .Plante G, et al. New Measurement of the Scintillation Efficiency of Low-Energy Nuclear Recoils in Liquid Xenon. *Phys. Rev. C* **84** (2011) 045805.
- 71 .Aprile E, et al. First Dark Matter Search Results from the XENON1T Experiment. *Phys. Rev. Lett.* **119** (2017) 181301. doi:10.1103/PhysRevLett.119.181301.
- 72 .Akerib DS, et al. Low-energy (0.7-74 keV) nuclear recoil calibration of the LUX dark matter experiment using D-D neutron scattering kinematics. *arXiv:1608.05381* (2016).
- 73 .Akerib DS, et al. Results from a Search for Dark Matter in the Complete LUX Exposure. *Phys. Rev. Lett.* **118** (2017) 021303. doi:10.1103/PhysRevLett.118.021303.
- 74 .Huang D. *Ultra-Low Energy Calibration of the LUX and LZ Dark Matter Detectors*. Ph.D. thesis, Brown U. (2020). doi:10.26300/zvs6-fx07.
- 75 .Akerib DS, et al. Improved Dark Matter Search Sensitivity Resulting from LUX Low-Energy Nuclear Recoil Calibration. *arXiv:2210.05859* (2022). doi:10.48550/ARXIV.2210.05859.
- 76 .Aprile E, Anthony M, Lin Q, Greene Z, de Perio P, Gao F, et al. Simultaneous measurement of the light and charge response of liquid xenon to low-energy nuclear recoils at multiple electric fields. *Phys. Rev. D* **98** (2018) 112003. doi:10.1103/PhysRevD.98.112003.
- 77 .Lenardo B, Xu J, Pereverzev S, Akindele OA, Naim D, Kingston J, et al. Measurement of the ionization yield from nuclear recoils in liquid xenon between 0.3 – 6 keV with single-ionization-electron sensitivity. *arXiv:1908.00518* (2019).
- 78 .Horn M, et al. Nuclear recoil scintillation and ionisation yields in liquid xenon from ZEPLIN-III data. *Physics Letters B* **705** (2011) 471–476. doi:10.1016/j.physletb.2011.10.038.

- 79 .Sorensen P, et al. Lowering the low-energy threshold of xenon detectors. *PoS IDM2010* (2011) 017. doi:10.22323/1.110.0017.
- 80 .Sorensen P, Dahl CE. Nuclear recoil energy scale in liquid xenon with application to the direct detection of dark matter. *Phys. Rev. D* **83** (2011) 063501. doi:10.1103/PhysRevD.83.063501.
- 81 .Faham C, Gehman V, Currie A, Dobi A, Sorensen P, Gaitskell R. Measurements of wavelength-dependent double photoelectron emission from single photons in VUV-sensitive photomultiplier tubes. *Journal of Instrumentation* **10** (2015) P09010–P09010. doi:10.1088/1748-0221/10/09/p09010.
- 82 .Edwards B, et al. Extraction efficiency of drifting electrons in a two-phase xenon time projection chamber. *JINST* **13** (2018) P01005. doi:10.1088/1748-0221/13/01/P01005.
- 83 .Xu J, Pereverzev S, Lenardo B, Kingston J, Naim D, Bernstein A, et al. Electron extraction efficiency study for dual-phase xenon dark matter experiments. *Phys. Rev. D* **99** (2019) 103024. doi:10.1103/PhysRevD.99.103024.
- 84 .Lindhard J. Range concepts and heavy ion ranges. *Mat. Fys. Medd. K. Dan. Vidensk. Selsk.* **33** (1963) 10.
- 85 .Sorensen P. Atomic limits in the search for galactic dark matter. *Phys. Rev. D* **91** (2015) 083509. doi:10.1103/PhysRevD.91.083509.
- 86 .Aprile E, et al. Search for Light Dark Matter Interactions Enhanced by the Migdal Effect or Bremsstrahlung in XENON1T. *Physical Review Letters* **123** (2019). doi:10.1103/physrevlett.123.241803.
- 87 .Hitachi A. Properties of liquid xenon scintillation for dark matter searches. *Astroparticle Physics* **24** (2005) 247 – 256. doi:http://dx.doi.org/10.1016/j.astropartphys.2005.07.002.
- 88 .Aprile E, Dahl CE, de Viveiros L, Gaitskell RJ, Giboni KL, Kwong J, et al. Simultaneous measurement of ionization and scintillation from nuclear recoils in liquid xenon for a dark matter experiment. *Phys. Rev. Lett.* **97** (2006) 081302. doi:10.1103/PhysRevLett.97.081302.
- 89 .Fano U. Ionization Yield of Radiations. II. The Fluctuations of the Number of Ions. *Phys. Rev.* **72** (1947) 26–29. doi:10.1103/PhysRev.72.26.
- 90 .Plante G. *The XENON100 Dark Matter Experiment: Design, Construction, Calibration and 2010 Search Results with Improved Measurement of the Scintillation Response of Liquid Xenon to Low-Energy Nuclear Recoils*. Ph.D. thesis, Columbia U. (main) (2012).
- 91 .Akerib DS, et al. Results of a Search for Sub-GeV Dark Matter Using 2013 LUX Data. *Phys. Rev. Lett.* **122** (2019) 131301. doi:10.1103/PhysRevLett.122.131301.
- 92 .Wang L, Mei DM. A Comprehensive Study of Low-Energy Response for Xenon-Based Dark Matter Experiments. *J. Phys. G* **44** (2017) 055001. doi:10.1088/1361-6471/aa6403.
- 93 .Akerib DS, et al. First results from the LUX dark matter experiment at the Sanford Underground Research Facility. *Phys. Rev. Lett.* **112** (2014) 091303. doi:10.1103/PhysRevLett.112.091303.
- 94 .Aprile E, et al. Excess electronic recoil events in XENON1T. *Phys. Rev. D* **102** (2020) 072004. doi:10.1103/PhysRevD.102.072004.
- 95 .Birks J. *The Theory and Practice of Scintillation Counting (Chapter 8 - Organic Liquid Scintillators)*. International Series of Monographs in Electronics and Instrumentation (Pergamon) (1964). doi:http://dx.doi.org/10.1016/B978-0-08-010472-0.50001-X.
- 96 .Mei DM, Yin ZB, Stonehill L, Hime A. A model of nuclear recoil scintillation efficiency in noble liquids. *Astroparticle Physics* **30** (2008) 12–17. doi:10.1016/j.astropartphys.2008.06.001.
- 97 .Sorensen P, et al. The scintillation and ionization yield of liquid xenon for nuclear recoils. *Nuclear Instruments and Methods in Physics Research Section A: Accelerators, Spectrometers, Detectors and Associated Equipment* **601** (2009) 339–346. doi:10.1016/j.nima.2008.12.197.

- 98 .Mu W, Xiong X, Ji X. Scintillation efficiency for low energy nuclear recoils in liquid xenon dark matter detectors. *Astroparticle Physics* **61** (2015) 56–61. doi:https://doi.org/10.1016/j.astropartphys.2014.06.010.
- 99 .Bezrukov F, Kahlhoefer F, Lindner M. Interplay between scintillation and ionization in liquid xenon dark matter searches. *Astroparticle Physics* **35** (2011) 119–127. doi:10.1016/j.astropartphys.2011.06.008.
- 100 .Mu W, Ji X. Ionization yield from nuclear recoils in liquid-xenon dark matter detection. *Astroparticle Physics* **62** (2015) 108–114. doi:https://doi.org/10.1016/j.astropartphys.2014.07.013.
- 101 .Sarkis Y, Aguilar-Arevalo A, D’Olivo JC. Study of the ionization efficiency for nuclear recoils in pure crystals. *Phys. Rev. D* **101** (2020) 102001. doi:10.1103/PhysRevD.101.102001.
- 102 .Lenardo B, Kazkaz K, Manalaysay A, Mock J, Szydagis M, Tripathi M. A Global Analysis of Light and Charge Yields in Liquid Xenon. *IEEE Trans. Nucl. Sci.* **62** (2015) 3387–3396. doi:10.1109/TNS.2015.2481322.
- 103 .Sorensen P. Anisotropic diffusion of electrons in liquid xenon with application to improving the sensitivity of direct dark matter searches. *Nuclear Instruments and Methods in Physics Research Section A: Accelerators, Spectrometers, Detectors and Associated Equipment* **635** (2011) 41–43. doi:10.1016/j.nima.2011.01.089.
- 104 .Akerib DS, et al. Improved Limits on Scattering of Weakly Interacting Massive Particles from Reanalysis of 2013 LUX Data. *Phys. Rev. Lett.* **116** (2016) 161301. doi:10.1103/PhysRevLett.116.161301.
- 105 .Mozumder A. Free-ion yield in liquid argon at low-LET. *Chemical Physics Letters* **238** (1995) 143–148. doi:10.1016/0009-2614(95)00384-3.
- 106 .Albert J, et al. Measurement of the Drift Velocity and Transverse Diffusion of Electrons in Liquid Xenon with the EXO-200 Detector. *Phys. Rev. C* **95** (2017) 025502. doi:10.1103/PhysRevC.95.025502.
- 107 .James R, Palmer J, Kaboth A, Ghag C, Aalbers J. FlameNEST: explicit profile likelihoods with the Noble Element Simulation Technique. *Journal of Instrumentation* **17** (2022) P08012. doi:10.1088/1748-0221/17/08/p08012.
- 108 .Biekert A, Chang C, Fink C, Garcia-Sciveres M, Glazer E, Guo W, et al. Scintillation yield from electronic and nuclear recoils in superfluid He-4. *Physical Review D* **105** (2022) 092005. doi:10.1103/physrevd.105.092005.
- 109 .Baudis L, Sanchez-Lucas P, Thieme K. A measurement of the mean electronic excitation energy of liquid xenon. *The Eur. Phys. Journal C* **81** (2021) 1060. doi:10.1140/epjc/s10052-021-09834-x.
- 110 .Acciarri R, et al. A study of electron recombination using highly ionizing particles in the ArgoNeuT Liquid Argon TPC. *JINST* **8** (2013) P08005. doi:10.1088/1748-0221/8/08/p08005.
- 111 .McMonigle R. *Updating Nuclear Recoil Models in the Noble Element Simulation Technique for the LUX-ZEPLIN Experiment*. Ph.D. thesis, UAlbany SUNY (2024).
- 112 .Abe S, et al. Search for the Majorana Nature of Neutrinos in the Inverted Mass Ordering Region with KamLAND-Zen. *Phys. Rev. Lett.* **130** (2023) 051801. doi:10.1103/PhysRevLett.130.051801.
- 113 .Albert JB, et al. Sensitivity and discovery potential of the proposed nEXO experiment to neutrinoless double- β decay. *Phys. Rev. C* **97** (2018) 065503. doi:10.1103/PhysRevC.97.065503.
- 114 .Akerib DS, et al. Projected sensitivity of the LUX-ZEPLIN experiment to the $0\nu\beta\beta$ decay of ^{136}Xe . *Phys. Rev. C* **102** (2020) 014602. doi:10.1103/PhysRevC.102.014602.
- 115 .Aprile E, et al. Double-weak decays of ^{124}Xe and ^{136}Xe in the XENON1T and XENONnT experiments. *Phys. Rev. C* **106** (2022) 024328. doi:10.1103/PhysRevC.106.024328.

- 116 .Aalbers J, et al. A Next-Generation Liquid Xenon Observatory for Dark Matter and Neutrino Physics. *Journal of Physics G: Nuclear and Particle Physics* **50** (2022) 013001. doi:10.1088/1361-6471/ac841a.
- 117 .Piazza O, Velan V, McKinsey D. A first principles approach to e-ion recombination in liquid Xe. *To be published* (2025).
- 118 .Rutkai G, Thol M, Span R, Vrabec J. How well does the Lennard-Jones potential represent the thermodynamic properties of noble gases? *Molecular Physics* **115** (2017) 1104–1121. doi:10.1080/00268976.2016.1246760.
- 119 .Bolotnikov A, Ramsey B. The spectroscopic properties of high-pressure xenon. *Nuclear Instruments and Methods in Physics Research Section A: Accelerators, Spectrometers, Detectors and Associated Equipment* **396** (1997) 360–370. doi:10.1016/S0168-9002(97)00784-5.
- 120 .Ahlen SP. Theoretical and experimental aspects of the energy loss of relativistic heavily ionizing particles. *Rev. Mod. Phys.* **52** (1980) 121–173. doi:10.1103/RevModPhys.52.121.
- 121 .Miyajima M, Takahashi T, Konno S, Hamada T, Kubota S, Shibamura H, et al. Average energy expended per ion pair in liquid argon. *Phys. Rev. A* **9** (1974) 1438–1443. doi:10.1103/PhysRevA.9.1438.
- 122 .Obodovskii IM, Pokachalov SG. (in Russian). *Soviet Journal of Low Temp. Phys.* **5** (1974) 829–836.
- 123 .Yoo J, Cease H, Jaskierny W, Markley D, Pahlka R, Balakishiyeva D, et al. Scalability Study of Solid Xenon. *JINST* **10** (2015) P04009. doi:10.1088/1748-0221/10/04/P04009.
- 124 .Takahashi T, Konno S, Hamada T, Miyajima M, Kubota S, Nakamoto A, et al. Average energy expended per ion pair in liquid xenon. *Phys. Rev. A* **12** (1975) 1771–1775. doi:10.1103/PhysRevA.12.1771.
- 125 .Obodovskii IM, Pokachalov SG. (in Russian). *Soviet Journal of Low Temp. Phys.* **5** (1979) 393.
- 126 .Doke T, Masuda K, Shibamura E. Estimation of absolute photon yields in liquid argon and xenon for relativistic (1 MeV) electrons. *NIM A* **291** (1990) 617–620.
- 127 .Doke T. A historical view on the R&D for liquid rare gas detectors. *NIM A* **327** (1993) 113–118. doi:https://doi.org/10.1016/0168-9002(93)91423-K.
- 128 .Tanaka M, Doke T, Hitachi A, Kato T, Kikuchi J, Masuda K, et al. LET dependence of scintillation yields in liquid xenon. *NIM A* **457** (2001) 454–463. doi:https://doi.org/10.1016/S0168-9002(00)00785-3.
- 129 .Shutt T, Dahl C, Kwong J, Bolozdynya A, Brusov P. Performance and fundamental processes at low energy in a two-phase liquid xenon dark matter detector. *NIM A* **579** (2007) 451–453. doi:https://doi.org/10.1016/j.nima.2007.04.104. Proceedings of the 11th Symposium on Radiation Measurements and Applications.
- 130 .Nygren D. High-pressure xenon gas electroluminescent TPC for zero-neutrino double-beta-decay search. *NIM A* **603** (2009) 337–348. doi:https://doi.org/10.1016/j.nima.2009.01.222.
- 131 .[Dataset] Szydajis M, et al. Noble Element Simulation Technique <https://zenodo.org/records/8215927> (2023). doi:10.5281/zenodo.8215927.

SUPPLEMENTARY MATERIAL

Appendix A: Work Function, Exciton-Ion Ratio, and Fano Factor

This appendix presents the origins of the density-dependent work function for total quanta W_q and the high- E asymptote of the exciton-to-ion ratio N_{ex}/N_i implemented within NEST, as well as the Fano-like factor for total quanta, all for ER. Note that Figure 6 uses a 21.8 eV normalization for W_i , reported as going to 1.00 as $\rho \rightarrow 0 \text{ g/cm}^3$ in [31] and [119]. That value is based upon averaging three values reported in the same sources without recorded error bars: 21.5 and 22.1 (originally from [120], and also the ICRU value) in the former source and 21.9 in the latter. It represents $1/Q_y$ as $\mathcal{E} \rightarrow \infty$. ($W_q < W_i$ by definition.)

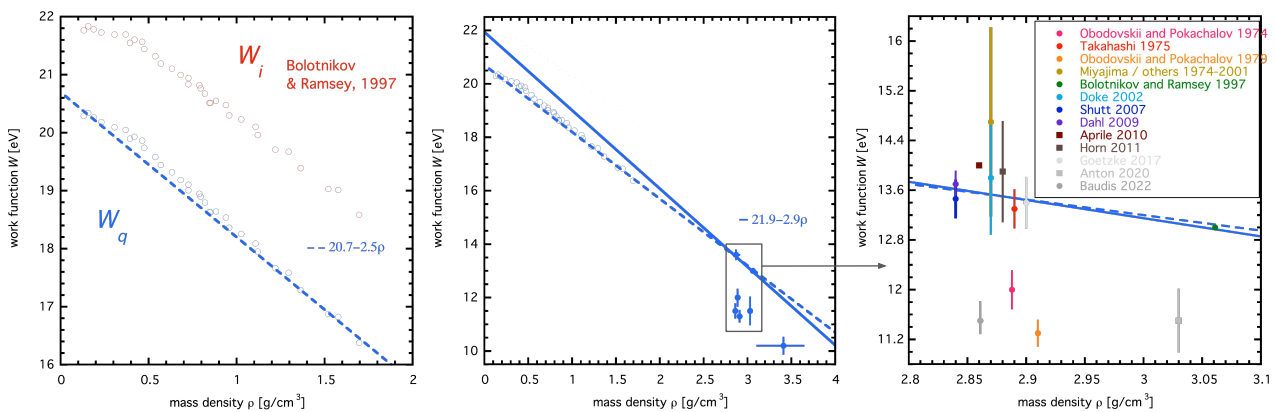


Figure 6. Left: The ionization work function, W_i , as a function of the density for GXe (gaseous Xe) as hollow red circles [119] normalized to $W_{i,0} = 21.8 \text{ eV}$, and converted to W_q in cyan based upon $N_{ex}/N_i = 0.0674 + 0.0397\rho$, the simplest way to account for a value of 0.06–0.07 for room-temperature/pressure gas [121] and the highest fit value for LXe at the highest E s in LXe, 0.20 [18]. That linear dependence of N_{ex}/N_i on ρ also serves to flatten the curvature of the W dependence, allowing for a linear fit, though with densities between 0.5 and 1 still “bulging” past the line (NEST previously utilized a sigmoid but abandoned it for simplicity, given the unknown errors on the data and an *ad hoc* exciton-ion ratio dependency.) Middle: the same corrected data repeated in cyan and same fit, but with data from condensed Xe (liquid and solid) added as solid circles. The only known data point for solid Xe [122] is the lowest / right-most, at an unknown ρ (taken to be 3.41 [123], but with an uncertainty spanning 3.1–3.64). The high- W_q point above 3 g/cm^3 without an error is part of the same [119] data set as the GXe points. A new two-point fit to only LXe data points, those agreeing on a higher W_q near 2.88 averaged together, and the single point at 3.06, is introduced as a solid cyan line (the original repeated as a dashed line). Due to the uncertainty in the normalization of the hollow circles (GXe) the new steeper line may still agree with them. Right: A blow-up of LXe data points, with all high- W_q points below 3 g/cm^3 that were merged (error-weighted average) into one point in the middle plot now separated, broken down by source in the legend: pink [122], red [124], orange [125], yellow [121, 126, 127, 128]. The remaining, from top to bottom, are: [119, 18, 129, 20, 44, 78, 25, 46, 109].

A reduction in W_q with density and between the gaseous and condensed phases is observed in nearly all noble elements [31], meaning it takes less E to either excite or ionize atoms as they get closer together. Additionally, N_{ex}/N_i appears to increase with ρ . This suggests that as mass density increases ionization density does as well, and recombination becomes stronger, resulting in a component of it that is near-immediate and can be modeled as direct excitation. This is known as Onsager or geminate recombination, and is effectively the opposite of volume or columnar recombination [57]. Another possibility, as mentioned in Section 2.2, is that W_i and W_{ex} must be considered separately. That would complicate the definition of a combined- E scale for energy reconstruction, useful for any phase. It relies on strict anti-correlation.

Next, we cover the Fano-like factor F_q for variation in total quanta in greater depth than in the main body of the text, plus the excitation / recombination fluctuations again. For the former, the origins of its density, field, and E dependences are presented in Figure 7 from left to right. Resolution here is defined as Gaussian width divided by median. The full width half max (FWHM) is used for the first plot, as that is how its data were originally reported, and standard deviation is used for the others. Results from ^{137}Cs are displayed, one of the most common past standard candles after ^{57}Co . Xe gas and supercritical fluid at room temperature but distinct pressures are represented in the left pane (up to > 60 bar, corresponding to about 1.8 g/cm^3) while the other two are for liquid, where the standard NEST recombination fluctuations for LXe ($\sigma_p = 0.04\text{--}0.09$) are applied, dependent on \mathcal{E} and E .

The recombination fluctuations, which become canceled out on a combined- E scale, were historically often conflated with F_q . Effective F_{ph} and F_{e-} (aka F_{sc} and F_i) can still be defined, with enormous but inconsequential values: 60 and 20 for the ^{137}Cs example, at 1000 V/cm in LXe, matching [130].

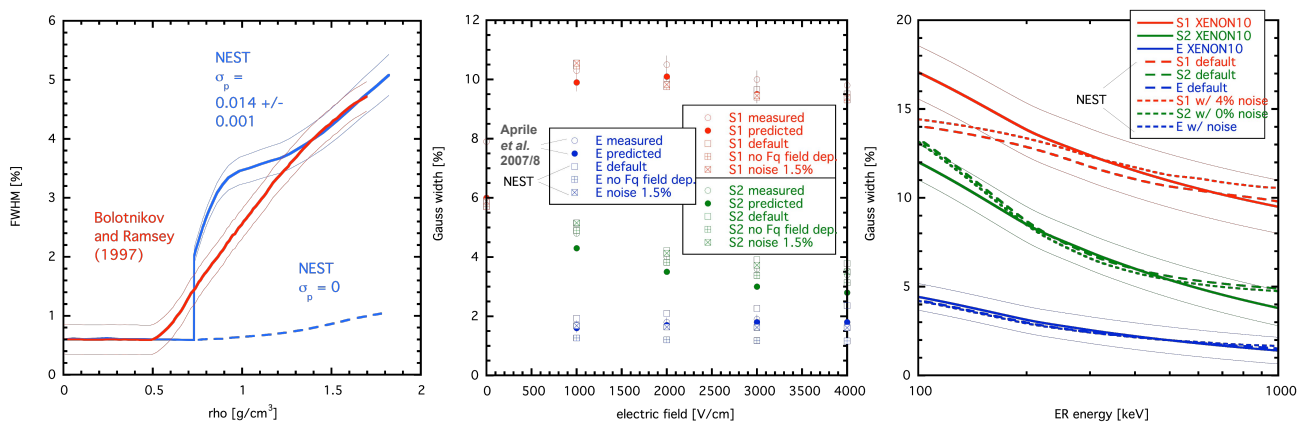


Figure 7. Left: The ionization-only resolution of ^{137}Cs gamma rays in GXe at 7 kV/cm vs. density [119] in red, with approximate error band (note: these same data feature prominently in [130]). At very low densities there is nearly no recombination: S1 comes only from excitations at this very high field, but N_{ex}/N_i is low too (near 0.06). Thus, resolution in this flat region is driven almost exclusively by low $F_q = 0.1 - 0.2 \lesssim F_i$. To follow F 's ρ dependence, featured in Eq. (7) in the main text, a cubic spline was fit to discrete F 's measured or predicted (calculated) for xenon as a low-pressure gas, supercritical fluid, liquid, and solid, featured in Table 2.4 of [31]. NEST (cyan) was intentionally not fit to the red, to see if it could be predicted. As a result it does not quite agree on the ρ at which resolution begins to depart from flatness, at $O(100)$ bar, and has some disagreement at moderate ρ s (though no actual major experiments operate under such conditions any longer). The dashed cyan line represents only binomial recombination fluctuations, with the closest fit to real data achieved with a non-zero value of the non-binomial contribution (solid lines) thus demonstrating that these matter even in a gas or a van der Waals fluid not just true liquid, at sufficiently high densities. Energy resolution is not driven by just F_q , when considering only a single channel such as ionization alone. Middle: Resolution as a function of \mathcal{E} for LXe (2.9 g/cm^3) for the same fixed $E = 662\text{ keV}$ and particle (γ) again, for both ionization (S2, green) and scintillation (S1, red) now, as well as for the combined- E scale (blue) that merges the information from both to create the best-possible resolution / lowest width [51]. Default NEST options reproduce real data well, but without the F_q square-root \mathcal{E} dependence from Eqn. (7) in the text the final resolution is seriously underestimated: 1.1–1.2 compared to 1.5–2.0% in reality. Another option for matching data with NEST is presented where $F_q \approx 0$ and linear noise terms are added to represent unknown detector effects, which the “predicted” points from Aprile were meant to address. In all NEST options presented, $g_1 = 0.05$, typical for the time of data collection, and 40 V/cm stands in for 0 V/cm (impossible to directly model within NEST, as explained in the text). Note that [119] also has LXe data, and found 2.9% (converted from FWHM) resolution at 7000 V/cm, in good agreement with the asymptotic behavior of the S2s seen in this plot. Right: With density (LXe) and field (730 V/cm) both fixed now this is the E dependence, for XENON10 [44]. Two NEST options are presented: the default, plus usage of Gaussian noise terms again, at $F_q = 0.03$ (no \mathcal{E} nor E dependence, only ρ). At 662 keV, the measured S1, S2, and total (E) resolutions were 10.8, 5.1, and 2.2%, respectively, all comparable to the 1 kV/cm results from the middle plot.

Appendix B: Tabulation of NEST Model Parameters

In this appendix, we provide tables detailing the functions and model parameters used in NEST for LXe yields from β ER, γ ER, NR, as well as their fluctuations. NEST has additional models for ^{83m}Kr ER as well as NR from non-Xe nuclei (including α decay), findable in code on GitHub [131].

Table 1. Table of NEST model parameters comprising the β ER yield models for charge, as shown in Equation (5), and light.

m_1	Stitching-region yield for β ER charge yields between low and high energies, depending on field and density: $m_1 = 30.66 + (6.20 - 30.66)/(1 + (\mathcal{E}/73.86)^{2.03})^{0.42}$ at a typical LXe density. Takes values $\mathcal{O}(10 \text{ keV}^{-1})$ for $\mathcal{O}(100 \text{ V/cm})$ fields.
m_2	Low-energy asymptote of the β ER charge yield equation. Default value is approximately 77.3 keV^{-1} .
m_3	Controls the energy-dependent shape of the β charge yields in the low-energy (Thomas-Imel) regime: $m_3 = \log_{10}(\mathcal{E}) \cdot 0.14 + 0.53$. Field-dependent function, with values of approximately 0.8-1.5 keV for $\mathcal{O}(100 \text{ V/cm})$ fields.
m_4	Field-dependent control on the energy-dependent shape of the β charge yields at lower energies: $m_4 = 1.82 + (2.83 - 1.82)/(1 + (\mathcal{E}/144.65)^{-2.81})$. Takes values from approximately 2.0-2.8 for $\mathcal{O}(100 \text{ V/cm})$ fields.
m_5	High-energy asymptote of the β charge yield model. Defined as: $m_5 = \frac{1}{W} \cdot [1 + N_{ex}/N_i]^{-1} - m_1$ (See Ref. [27].)
m_6	Low-energy asymptote of the higher-energy behavior for β ER charge yields. Degenerate with m_1 and explicitly set to 0 keV^{-1} .
m_7	Field-dependent scaling on the behavior of the β charge yields at higher energies: $m_7 = 7.03 + (98.28 - 7.03)/(1 + (\mathcal{E}/256.48)^{1.29})$. Takes values $\mathcal{O}(10 \text{ keV})$ for $\mathcal{O}(100 \text{ V/cm})$ fields.
m_8	Control on the energy-dependent shape of the β charge yields at higher energies. The default value is a constant, 4.3.
m_9	Asymmetry control on the low-energy behavior. The default value is a constant, 0.3.
m_{10}	Asymmetry control on the high-energy behavior of the β charge yields model: $m_{10} = 0.05 + (0.12 - 0.05)/(1 + (\mathcal{E}/139.26)^{-0.66})$. Field-dependent function that takes values ~ 0.1 for $\mathcal{O}(100 \text{ V/cm})$ fields.

Table 2. Table of NEST model parameters comprising the γ ER yield models for light and for charge, reusing Equation (5) from the β ER yields.

m_1	Field-dependent function controlling the transition between lower and higher energies: $m_1 = 34.0 + (3.3 - 34.0)/(1 + (\mathcal{E}/165.3)^{0.7})$.
m_2	Low-energy asymptote of the γ ER charge yield equation, defined as $1/W_q$ in units of keV^{-1} .
m_3	Controls the energy-dependent shape of the γ charge yields in the low-energy (Thomas-Imel) regime; a constant value of 2 keV is used.
m_4	Control on the energy-dependent shape of the γ charge yields at lower energies; a constant power of 2 is used.
m_5	High-energy asymptote of the γ charge yield model. Defined as: $m_5 = 23.2 + (10.7 - 23.1)/(1 + (\mathcal{E}/34.2)^{0.9})$.
m_6	Low-energy asymptote of the higher-energy behavior for γ ER charge yields. Degenerate with m_1 and explicitly set to 0 keV^{-1} .
m_7	Field-dependent and density-dependent scaling on the behavior of the γ charge yields at higher energies: $m_7 = 66.8 + (829.3 - 66.8)/(1 + (\rho^{8.2} \cdot \mathcal{E}/(2.4 \cdot 10^5))^{0.8})$.
m_8	Control on the energy-dependent shape of the γ charge yields at higher energies. Default value is a constant power of 2.
m_9	Asymmetry control on the low-energy behavior: unused for γ ER yields and set to unity.
m_{10}	Asymmetry control on the high-energy behavior of the γ charge yields model: unused for γ ER yields and set to unity.

Table 3. Table of NEST model parameters comprising the NR mean yield models: for total quanta, charge, and light, as shown in Equations (9), (12), and (13).

a	Scaling on NR total quanta. Default value is $11^{+2.0}_{-0.5} \text{ keV}^{-b}$.
b	Power-law exponent for the NR total quanta. Default value is 1.1 ± 0.05 .
ς	Field dependence in NR light and charge yields, with mass-density-dependent scaling (Equation (11)).
ρ_0	Reference density for scaling density-dependent NEST functions: 2.90 g/cm^3 .
v	Hypothetical exponential control on density dependence in ς ; the default value is 0.3.
γ	Power-law base for the field dependence in ς . Default value is 0.0480 ± 0.0021 .
δ	Power-law exponent in the field dependence in ς ; default value is -0.0533 ± 0.0068 .
ϵ	Reshaping parameter for NR charge yields, controlling the effective energy scale at which the charge yield behavior changes. The default value is $12.6^{+3.4}_{-2.9} \text{ keV}$.
p	Exponent which controls the shape of the energy dependence of the NR charge yields at energies greater than $\mathcal{O}(\epsilon)$. Default value is 0.5.
ζ	Controls the energy dependence of the NR charge yields roll-off at low energies. Default value is $0.3 \pm 0.1 \text{ keV}$.
η	Controls energy-dependent shape of the NR charge yields roll-off at low energies. Default value is 2 ± 1 .
θ	Controls the energy dependence of the NR light yields roll-off. Default value is $0.30 \pm 0.05 \text{ keV}$.
ι	Controls the shape of the energy dependence of the NR light yields roll-off. Default value is 2.0 ± 0.5 .

Table 4. Table of NEST model parameters for different types of fluctuations for ERs and NRs.

F_q	Fano-like factor for statistical fluctuations. For ERs, this is proportional to $\sqrt{E \cdot \mathcal{E}}$; see Equation (7). For NRs, this is separated into fluctuations for N_{ex} and N_i ; the default value is 0.4 for both in NEST v2.3.11, while the values were 1.0 in previous NEST versions. (F_{ex} was underestimated to be conservative for low-mass WIMPs.)
σ_p	Non-binomial contribution to recombination fluctuations, modeled as a skew Gaussian in electron fraction space.
A	Amplitude of non-binomial recombination skew Gaussian. For NRs, this is a constant 0.04 (v2.3.11) or 0.1 (v2.3.10). For ERs, it is field-dependent: $A = 0.09 + (0.05 - 0.09)/(1 + (\mathcal{E}/295.2)^{251.6})^{0.007}$, where 0.05 was 0.055 in 2.3.10
ξ	Centroid-location parameter of the non-binomial recombination skew Gaussian. Default value for ERs is an electron fraction of 0.45, but 0.5 for NRs.
ω	Width parameter for the non-binomial recombination skew Gaussian. Takes value of 0.205 for ERs and 0.19 for NRs.
α_p	Skewness parameters for the non-binomial recombination skew Gaussian. Takes the value -0.2 for ERs, while being zero for NRs.
α_r	Additional skewness in the recombination process itself. Field- and energy- dependent equations can be found in Ref. [59] for ERs, while this is fixed at 2.25 for NRs, with evidence of higher values in [59].